Machine learning in reservoir rocks characterization: Integrating seismic data resolution-enhancement for seismic facies classification

by

Papa Amoo Owusu

B.S., University of Ghana, 2017

A THESIS

submitted in partial fulfillment of the requirements for the degree

MASTER OF SCIENCE

Department of Geology
College of Arts and Sciences

KANSAS STATE UNIVERSITY
Manhattan, Kansas

2023

Approved by:

Major Professor
Dr. Abdelmoneam Raef

Copyright

Abstract

Amid increasing interest in the dual enhanced oil recovery (EOR) and carbon geological sequestration (CGS) programs, improved static reservoir models emerge as a requirement for well-guided decision-making pertaining to the design of injector-producer well-drilling patterns. To this end, this study utilizes unsupervised machine learning approach leveraged with seismic resolution data preconditioning and spectral analysis to evaluate seismic facies based on machine learning models of clustering in multi-attributes space of the Mississippian carbonates of Kansas. The study provides a benchmark for understanding seismic facies distribution and implications for reservoir aspects pertaining to Enhanced Oil Recovery (EOR) and/or Carbon Geological Sequestration (CGS) programs, especially when encountering sparse well-logs control. A 3D seismic reflection P-wave data and a suite of well-logs and drilling reports constitute the data used for seismic facies based on seismic attributes input to machine learning hierarchical analysis and K-means clustering models. The results of seismic facies, six facies clusters, are analyzed in integration with the target-interval estimated mineralogy (Calcite-Dolomite-Quartz) and a predicted reservoir porosity. The study unravels the nature of the seismic (litho)facies interplay with porosity, sheds light on interpreting unsupervised machine learning classification of Kansas Mississippian carbonates at multi-resolution levels, and paves the way for an improved static model to enable effective CO2-EOR and geosequestration decision making.

Table of Contents

List of Figures

Chapter 1 - Introduction

Fossil energy generated CO2 still constitute a significant percentage of the global anthropogenic CO2 released into the atmosphere (Bickle, 2009; O'Neill, 2020). Despite efforts to diversify the international energy mix by developing other energy sources such as wind, solar, and nuclear, fossil fuels offer relatively cheap and reliable energy to developed and developing economies worldwide. Owing to this, Carbon Capture and Storage (CCS) systems development has a pivotal role in ensuring fossil energy is optimally harnessed without significant emission of CO2 into the atmosphere (Baines & Worden, 2004; Buchanan & Carr, 2008). In addition, geological formations such as depleted hydrocarbon reservoirs or saline aquifers, deep oceans and sea beds, coal seams, and methane hydrates provide prospective sites for CO2 geosequestration and enhanced oil recovery (EOR) (Shulakova et al., 2017; Siqueira et al., 2017).

Based on existing knowledge, Bickle (2009) ranks storage in depleted hydrocarbon reservoirs and saline aquifers as the best option, such as storing natural gas in reservoirs and using CO2-EOR to optimize producing fields. However, the limitations stem from scalability in terms of cost and storage timescale of the geological formations. Another challenge is the storage capacity of reservoirs arising from heterogeneities and sealing rock formation integrity (Bickle, 2009; Tan et al., 2022). Carbonate reservoirs, though, form about 60% of hydrocarbon reservoirs; they exhibit complex heterogeneities making it challenging to characterize the petrophysical and lithological variations (Shulakova et al., 2017; Tan et al., 2022). Notwithstanding the challenges, the storage volume capacity for CO2-EOR and geosequestration underpins the need to incorporate more sophisticated techniques to characterize carbonate reservoirs (Masaferro et al., 2003).

Seismic data volumes and functional attributes available with time have increased in size such that conventional workflows used by human interpreters cannot exploit them for maximum inference of the subsurface heterogeneities. Chopra and Marfurt (2020) explain that the size of seismic surveys has increased to the tune of megamerger and larger gigamerge; hence, interpretation workflows likely require the integration of terabytes of data to delineate reservoir heterogeneities to the best of detail. Therefore, there is a need to incorporate machine learning techniques into conventional interpretation workflows to maximize the quality of subsurface geological information derived from seismic reflection datasets.

This study utilizes unsupervised machine learning, resolution enhancement of 3D seismic reflection data, and petrophysical logs to build a representative seismic facies map for the Mississippian reservoir in the Wellington field and Anston-Bates area, Sumner County, Southcentral Kansas, as a potential site for CO2-EOR and GCS.

Problem Statement

The Mississippian carbonate reservoir within the Wellington and Anston-Bates fields, Sumner County, is marked as a potential zone for commercial-scale CO2-EOR and geosequestration in Kansas by the US Department of Energy (DOE) and the Kansas Geological Survey (KGS) (Watney et al., 2011). The problem stems from the Mississippian carbonate reservoir exhibiting complex spatial heterogeneities owing to dolomitization, silicification, and other diagenetic processes. This study uses seismic data and suitable machine learning clustering techniques to characterize the reservoir facies heterogeneities of the Mississippian carbonate to a representative level. These facies models will provide a base to effectively model CO2 flow under supercritical conditions and plan optimal injection wells in the reservoir.

Relevant Previous Seismic Reflection Studies

Ohl and Raef (2014) characterized prominent geological structures within the Wellington field and their controls on the spatial distribution of petrophysical facies. Geophysical well logs and 3D seismic reflection data were used in the study to characterize the Mississippian reservoir and Arbuckle aquifer to understand CO2 flood and migration pathways within them. The geological structures were delineated by three seismic attributes: the most negative curvature, seismic amplitude, and coherency. In addition, petrophysical seismic facies modeling of the two horizons of interest was undertaken using an artificial neural network in a supervised classification setting. Three seismic amplitude attributes (energy, bandwidth, and peakedness) were extracted for each formation as inputs for the neural networks. On the other hand, three porosity classes obtained from neutron porosity well logs penetrating the horizons were used as targets for classification.

The structural attributes extracted for both horizons highlighted three NNE-SSW trending faults in the northern portion of the survey area. Based on the trends, Ohl and Raef (2014) inferred that the faults are associated with the Nemaha Uplift events, which must have occurred post-Mississippian deposition. Moreover, on the southern portion of the survey area, a seismic amplitude anomaly coincided with another NNE-SSW trending fault delineated only on the structural attribute maps of the Mississippian horizon. Seismic sections taken across the anomaly showed amplitude-dimming features. This was attributed to porosity variations due to lithofacies reworking by a reactivated fault within the Mississippian formation. The study concluded that the lineaments delineated in the study area influenced the petrophysical facies variation in the formations of interest. They also recommended increasing the number of seismic waveform attributes and neural networks to highlight better the spatial variation of porosity within the

formation and undertaking fault seal analysis to successfully model CO2 plume migration and flood within these formations.

Rijfkogel (2020) also utilized seismic attributes to characterize the spatial variability of facies(porosity) within the reservoirs of the Wellington field. He incorporated computed tomography scans on core samples from two wells to elucidate further vertical and lateral rock heterogeneities within the Mississippian reservoir's top, middle, and bottom intervals. For Wellington KGS 1-32 well, limestone, dolomite, and chert dominated the facies composition, with chert composition decreasing with depth in the reservoir. The porosities within the well vary from a combination of vuggy porosity and fracture-induced slit-shaped porosity at the top to only fracture-induced slit-shaped porosity at the bottom of the well. Conversely, the Wellington KGS 2-32 well contains autoclastic brecciated dolomite and limestone clast facies dominant at the top, with chert only encountered at the bottom. The porosities within the well vary from fracture-induced slit-shaped porosity at the top to a combination of slit-shaped porosity with few vuggy porosities at the bottom zone. He affirmed that the slit-shaped porosities result from fault reactivation related to the Nemaha uplift, whereas the vuggy porosities are attributed to the diagenesis of dolomite.

Chapter 2 - Geological Setting and Background

Tectonics

During the Mississippian period, the combined effect of the Acadian, Antler, and proto-Ouachita orogenies altered the paleogeography of North America, leaving tectonic remnants such as the Transcontinental Arch striking southwest-northeast and the east-southeast Burlington shelf (Gutschick & Sandberg, 1983; Lane & De Keyser, 1980; Wethington & Pranter, 2018; Wilson et al., 2019) (Fig. 2.1). Lane and De Keyser (1980) described the Transcontinental Arch as a Precambrian-aged ancient wrench fault system comparable to the San Andreas system of California. The Mississippian carbonates of the central United States, including the study area, form part of the Burlington shelf, whose depositional strike parallels the low but subaerial, southwest-northeast trending Transcontinental Arch (Gutschick & Sandberg, 1983; Lane & De Keyser, 1980). Although the general depositional system of the Mississippian is highly debatable, Wilson et al. (2019) summarize the various positions held by previous researchers broadly into a carbonate shelf (Burlington shelf), a possible carbonate shelf with no discernable shelf edge, and a ramp to distally steepened ramp environment.

The Mississippian reservoirs are partly sealed by the major unconformity separating deposits of Mississippian and Pennsylvanian ages, with the majority of 'chat' fields occurring in an arcuate fairway along the flanks of the south plunging Pratt anticline (Fig. 2.2) (Montgomery et al., 1998; Watney et al., 2001). The south plunging Pratt anticline is an extension of the Central Kansas uplift lineament, which separates the Sedgwick basin to the east and the Hugoton embayment to the west. During the early to middle Paleozoic, it formed part of the shelf region of the Anadarko Basin. The tectonic history associated with the Central Kansas uplift-Pratt anticline structure involves the Ouachita collision event, which resulted in fault-induced uplift

and tilting of strata followed by a prolonged period of erosion recorded as the regional unconformity separating the strata of Mississippian and Pennsylvanian age (Montgomery et al., 1998; Wilson et al., 2019). Two main thoughts on the genesis of the chert in reservoirs within the Osagean strata of the Mississippian system are penecontemporaneous deposition of carbonate facies rich in biogenic silica or fluid-induced diagenesis relating to meteoric water, groundwater movement, or hydrothermal alteration (Mazzullo et al., 2019; Watney et al., 2001). The Mississippian system's early inner ramp lithofacies were partly to extensively dolomitized as the sediments were still porous and permeable. Evidence of a late phase of dolomitization also exists in the system (Wilson et al., 2019). The reservoir properties of the Mississippian were ultimately altered by the combined effects of silicification(chert) and dolomitization (Watney et al., 2001).

Stratigraphy

The stratigraphy of the Mississippian system in Kansas is classified into four units; Kinderhookian (oldest), Osagean, Meramecian, and Chesterian (youngest)(Fig. 3). Mazzullo et al. (2019) describe the depositional geometry as aggradational for the lower Mississippian group, followed by progradational for the middle to the upper Mississippian group. The Osagean strata comprise the low resistivity, high porosity chert-rich formations(‘chat’), the most prolific hydrocarbon reservoirs in south-central Kansas (Watney et al., 2001). It is among the most complex carbonate reservoirs in the United States, owing to its depositional and diagenetic history (Montgomery et al., 1998; Watney et al., 2001). The Osagean stratal composition includes partly dolomitized cherty skeletal packstones, grainstones, argillaceous wackestones, and mudstones.

Although the Osegean strata outcrop only in the extreme southeast portion of Kansas, it is highly correlatable over the subsurface with significant lithofacies shift from clean mixed carbonate deposits at the northern part to cherty limestone, dolomite facies at the southern extent of Kansas (Montgomery et al., 1998; Watney et al., 2001; Wilson et al., 2019).

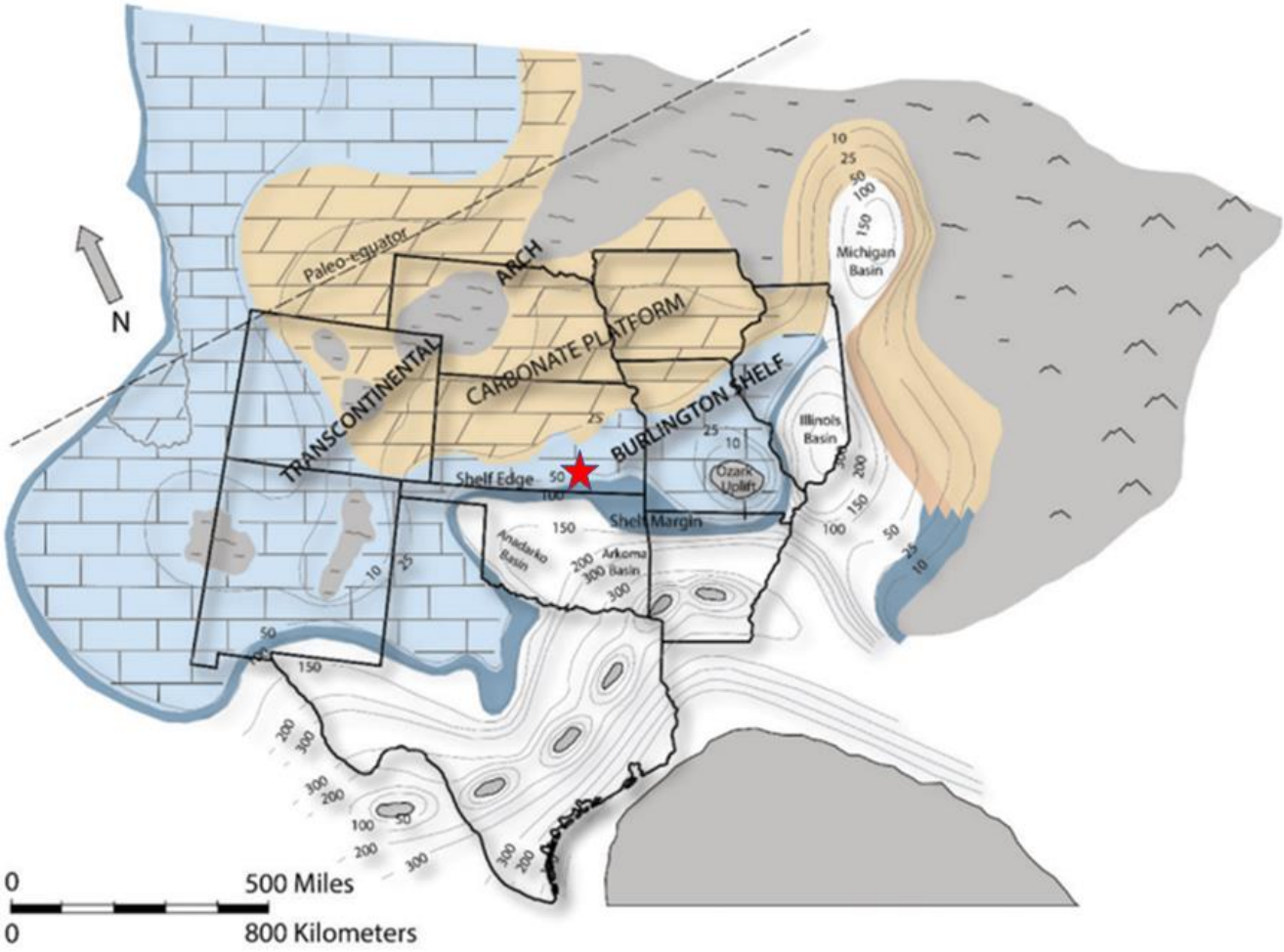

Figure 2.1. Generalized static paleo-depositional model of the midcontinent showing principal tectonic elements during the Mississippian time after Wilson et al. (2019). The red star marks Sumner County, Southcentral, Kansas, where the study area is located.

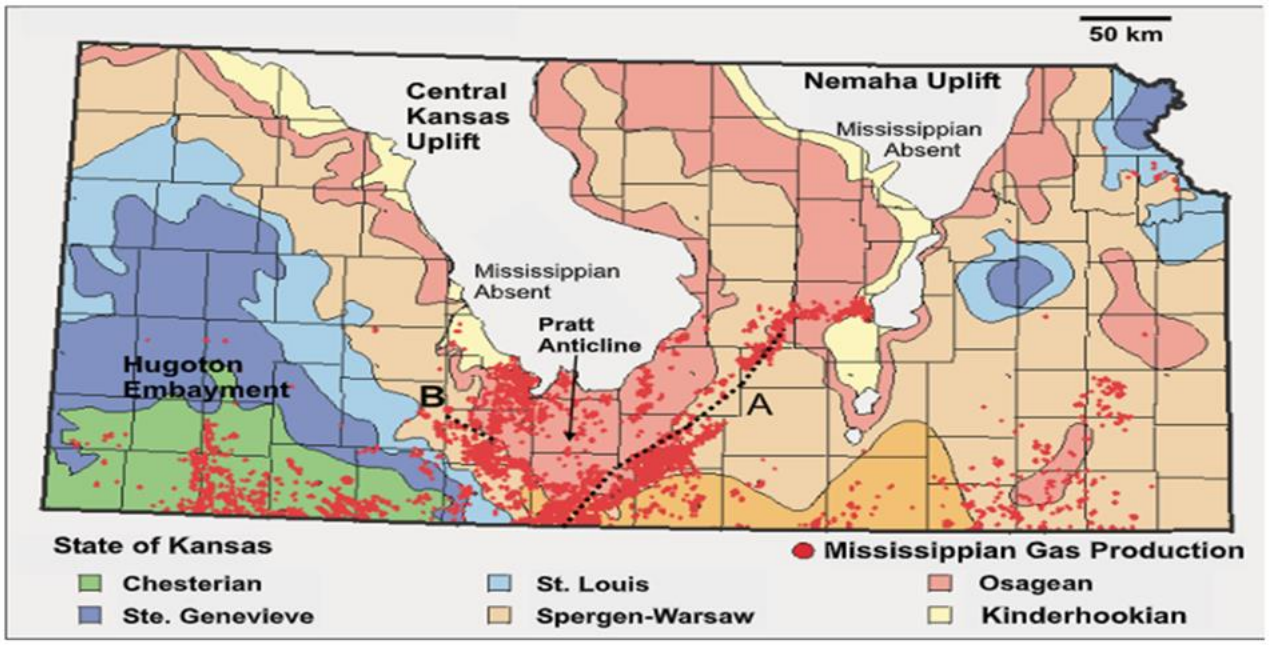

Figure 2.2 Geological map showing the Mississippian strata and existing geological structures (the dotted lines marked A and B are significant basement lineaments) (Watney et al., 2001).

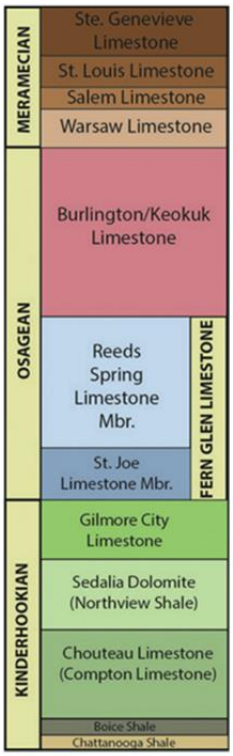

Figure 2.3 Generalized Stratigraphy of the Mississippian System in Kansas (Wilson et al., 2019).

Seismic Attributes and Seismic Resolution Enhancements

Seismic attributes offer valuable insights into seismic data for reservoir characterization, especially in hydrocarbon exploration. Subtle geologic structures, stratigraphic features, thin beds, and spatial distributions of reservoir petrophysical properties have been delineated from a single attribute or a combination of seismic attributes. Brown (2001) describes seismic attributes as not unique information but simply different displays of the basic information such as time, frequency, amplitude, phase, and attenuation encoded in seismic data. Even with the abundance of seismic attributes available in various commercial geophysical software suites, most offer similar information leading to redundancy if not carefully selected. Therefore, these attributes' statistical and geological correlation should be tested to choose optimal arrays of seismic attributes for reservoir or subsurface characterization (Barnes, 2006; Brown, 2001; J. Liu et al., 2018).

Seismic resolution remains crucial for evaluating seismic data quality in delineating reservoir bed boundaries and amplitude signatures correlative to fluid effect and petrophysical properties. It is influenced by multiple factors such as sampling density, source energy spectrum, signal-to-noise ratio, and low-frequency bandwidth of source energy (Reilly et al., 2023). The frequency bandwidth of seismic data can be enhanced with techniques such as spectral whitening, and spectral decomposition improves the resolution of thin beds (Chopra et al., 2006, 2010).

Zheng (2020) describes spectral whitening as the regional energy equalization of seismic signals to broaden the frequency bandwidth of the data. This is done in the time or frequency domain using the Fourier transform (Yilmaz, 2001). Spectral whitening enhances resolution and

attenuates low-frequency coherent noise (Manenti et al., 2018). However, the limitation of spectral whitening results in the amplification of high-frequency noise (Chopra et al., 2010).

Spectral decomposition enables discrete frequency slices/volumes of the original seismic frequency bandwidth to be taken to visualize subtle geological features masked in the original amplitude spectrum due to tuned reflections (Chopra & Marfurt, 2008; Partyka et al., 1999). Partyka et al. (1999) introduced spectral decomposition mainly to delineate and quantify thin bed thickness below the original seismic resolution. Notwithstanding, it has proven helpful in vast aspects of seismic studies spanning from fault characterization, lateral and vertical variation of reservoir facies, and reservoir fluid effect to AVO studies (Burnett et al., 2003; Burns & Street, 2005; Chen et al., 2008; Jung Yoon & Farfour, 2012).

Machine Learning in Reservoir Characterization

Large corporations such as Google and Amazon have successfully employed computer pattern recognition and classification systems since 2015 and are increasingly gaining ground in geoscience (Zhao et al., 2015). Particularly in seismic facies characterization and interpretation, increasing 3D seismic data volumes and resolution have contributed to the application of various machine learning methods (Chopra & Marfurt, 2020; Wrona et al., 2018). Fundamentally, machine learning encompasses the ability of computers to make predictions and identify complex hidden patterns by learning from data using various computational methods or concepts (El Bouchefry & de Souza, 2020).

Machine learning techniques are broadly grouped as supervised and unsupervised learning. Supervised learning involves exposing computer algorithms to training datasets that consist of inputs(features) and outputs(targets) to enable the algorithms to establish the best

mathematical relation that defines the targets using the features. For example, some supervised learning algorithms used in seismic facies classification include Artificial Neural Networks (ANN), Support Vector Machines (SVM), Random forest, K-nearest neighbor (KNN), and Gradient boosting (Wrona et al., 2018; Zhao et al., 2015). Seismic attributes are extracted as inputs for training, whereas well logs and production data are utilized to delineate facies classes as targets.

On the other hand, unsupervised learning employs clustering algorithms to delineate hidden classes in datasets devoid of predefined targets. Some clustering algorithms include the simple Cross plotting method, K-means clustering, Hierarchical clustering, Self-organizing maps (SOM), Principal component analysis (PCA), and Generative Topographic Mapping (GTM) (Belyadi & Haghighat, 2021; Hartigan, 2015). Although clustering algorithms can delineate several facies classes in seismic facies classifications, the challenge lies in correlating such facies classes with existing geological formations (Chopra & Marfurt, 2020; Zhao et al., 2015).

Hierarchical Clustering

This clustering method is unique because it produces a hierarchy or tree of clusters instead of a single set of clusters (Theodoridis & Koutroumbas, 2009). There are two main approaches to hierarchical clustering: the divisive (single large cluster to smaller finer clusters) and the agglomerative clustering(vice-versa) (Belyadi & Haghighat, 2021; El Bouchefry & de Souza, 2020; Hartigan, 2015).

The agglomerative clustering algorithm has been used in some seismic facies classification projects, for example (Liu et al., 2020; Sabeti & Nadjar, 2011; Wang, 2012). The agglomerative clustering algorithm can be computed by graph theory or matrix theory concepts

(Theodoridis & Koutroumbas, 2009). In the matrix theory concept, for a feature set of size *M X N*, where *M* is the number of data points, and *N* is the number of feature vectors, a dissimilarity matrix of size *M X M* is obtainable using vector distance measurements such as Euclidean distance and *M* becomes the number of single clusters also known as singletons. Iteratively, the singletons are paired in hierarchy till a single large cluster is obtained using linkage algorithms. Some linkage algorithms are Single linkage, Complete linkage, Average linkage, and Ward's linkage (de Amorim, 2015; Sabeti et al., 2011; Theodoridis & Koutroumbas, 2009). These linkages are computed as;

$$Single\ linkage = min_{x,y}\{d(x,y)|x \in C_a, y \in C_b\} \quad (1)$$

$$Complete\ linkage = max_{x,y}\{d(x,y)|x \in C_a, y \in C_b\} \quad (2)$$

$$Average\ linkage = \frac{1}{n_{C_a} n_{C_b}} \sum_{i=1}^{n_{C_a}} \sum_{j=1}^{n_{C_b}} d(x,y)|x \in C_a, y \in C_b \quad (3)$$

$$Ward's\ linkage = \frac{n_{C_a} n_{C_b}}{n_{C_a} + n_{C_b}} \left\| m_{C_a} - m_{C_b} \right\|^2 \quad (4)$$

Where *Ca* and *Cb* are clusters, *x,* and *y* are data points(singletons) within cluster *Ca* and *Cb* respectively, *d(x, y)* is dissimilarity distance, *nca* and *ncb* are the total number of data points (singletons) in clusters *Ca* and *Cb*, and *mca* and *mcb* are the vector means(centroids) of clusters *Ca* and *Cb*.

K-means Clustering

This method is one of the oldest and most widely used clustering algorithm due to its simple but powerful computation design (Belyadi & Haghighat, 2021). K-means clustering approach has been employed in some seismic facies characterization studies with plausible outcomes (Barnes & Laughlin, 2002; He et al., 2018; Song et al., 2018). The generic or base K-

means as a partitioning algorithm performs better for datasets with isotropic clusters and vice versa with noisy datasets or datasets with outliers (Maimon & Rokach, 2010). However, a significant limitation of this algorithm is the predefinition of number clusters (K), which is the main criteria to determine whether the algorithm reaches a local or global minimum in terms of convergence (that is, the sum of in-cluster distances from centroids) (Ming & Chiang, 2010). This issue of randomized selection of k-clusters in the algorithm is highly improved by modifications such as the K-means++ algorithm, which only requires one random cluster centroid selection and the subsequent cluster centroids selected based on a probability equal to the squared distance of the data point from the existing cluster point (Arthur & Vassilvitskii, 2006).

Chapter 3 - Data and Methods

Seismic Reflection Data

Data Acquisition and Description

This study utilized a merged 3-D P-wave seismic reflection data volume covering the Wellington Field and Anson-Bates area (Fig. 3.1). The seismic data set was acquired for the US Department of Energy (DOE) project (DE-FE0002056) with emphasis on geological carbon sequestration in the Mississippian carbonate reservoir with combined EOR and in the saline aquifer of the Arbuckle Group. The data consists of 288 inlines and 178 crosslines, with an acquisition geometry of bin size 82.5ft x 82.5ft. The data length is 2 seconds, and a sampling rate of 2ms was used in the acquisition. The data also had an original spectral bandwidth of 25 to 60 Hz.

Synthetic Modeling and Horizon Mapping

The Wellington-Anson-Bates 3D P-wave seismic reflection dataset and wells drilled in the study area were loaded into the IHS kingdom software. In addition, geophysical well logs and well top data of the Mississippian formation available for each well were also loaded into the software. First, a reflectivity coefficient was calculated for every depth point along the well from the density and sonic logs. Second, a zero-phase wavelet was extracted from a 7x7 seismic grid of inlines and crosslines around the Wellington KGS 1-32 well (Fig. 3.2). Finally, a 1D synthetic seismic trace was generated along the well by convolving the reflectivity coefficient calculated with the extracted zero-phase wavelet. The 1D synthetic seismic trace model built for the Wellington KGS 1-32 well provided an interval velocity model and established a suitable time-depth relationship to extrapolate the Mississippian top from the well to the corresponding peak

seismic reflector (Fig. 3.3). Tracing the peak seismic reflector, the Mississippian reservoir horizon was mapped to generate a time structure map to visualize the spatial variation in relief of the Mississippian reservoir in the study area The zero-crossing horizons above (trough-to-peak transition) and below (peak-to-trough transition) the reservoir peak horizon were also mapped for interval rms seismic attribute extraction (Fig. 3.4).

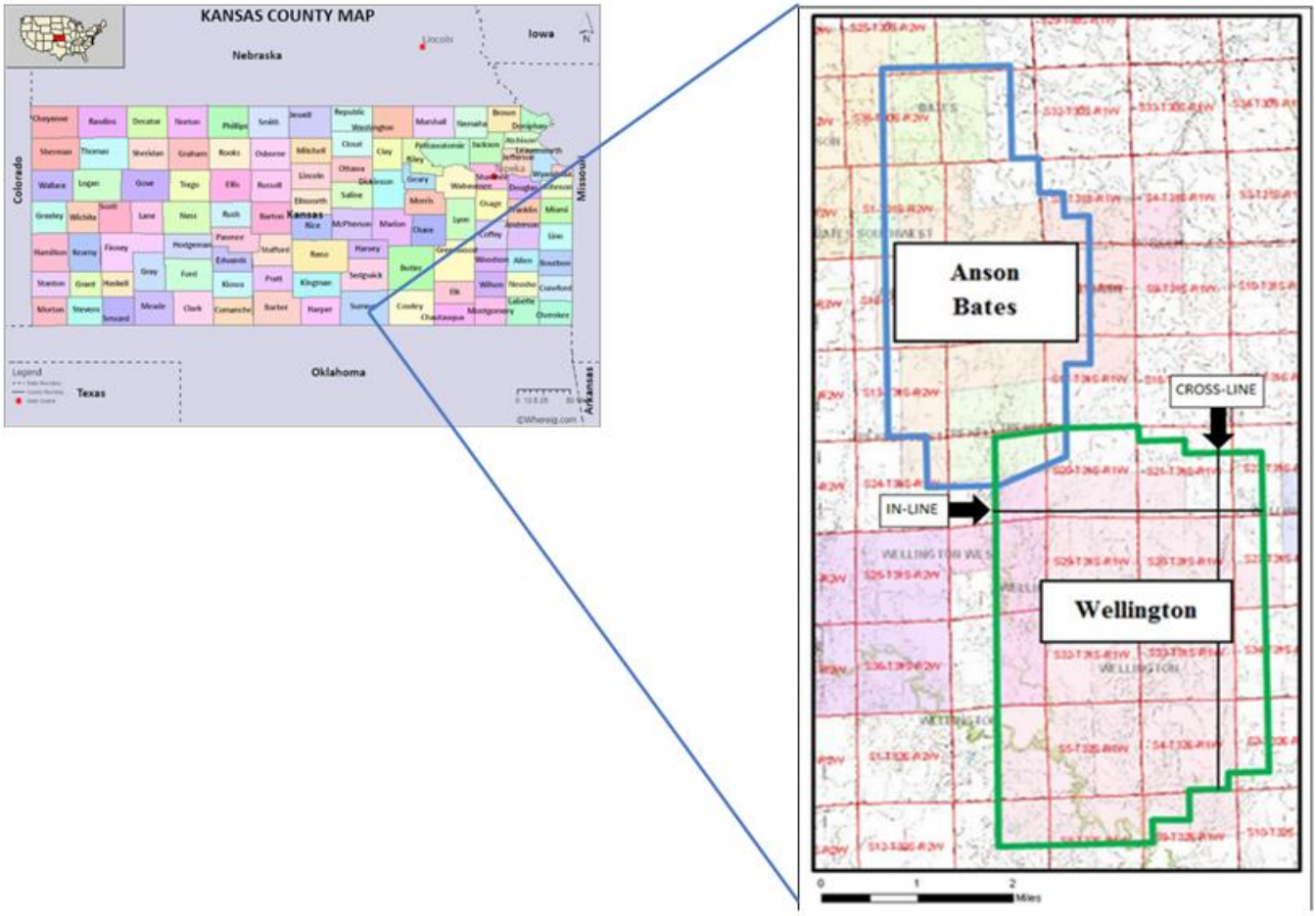

Figure 3.1 Seismic Survey map of the study area in Kansas after Ohl & Raef (2014).

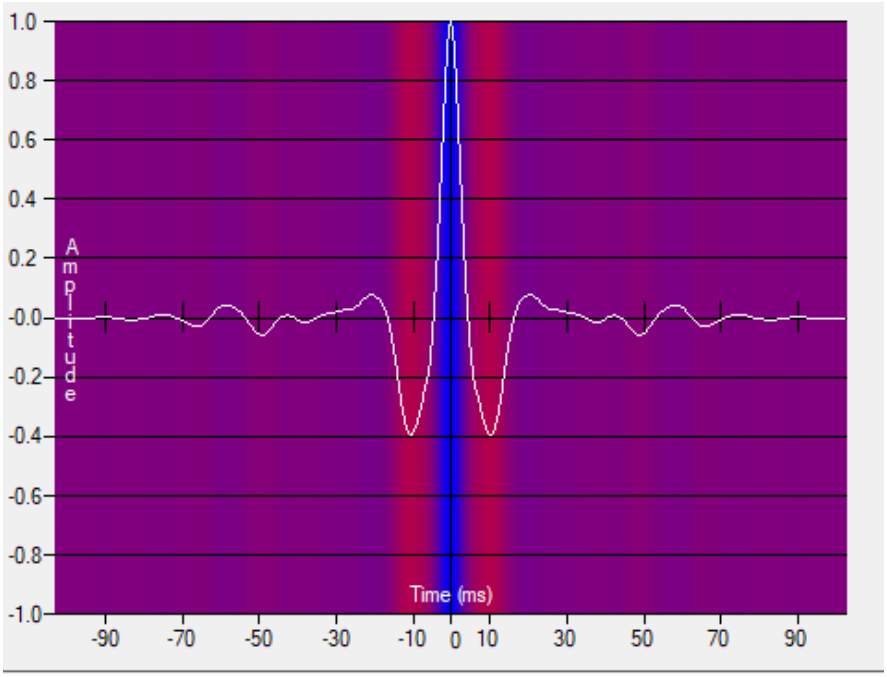

Figure 3.2 Zero-phase wavelet extracted from seismic grid around Wellington KGS 1-32 well for synthetic modeling.

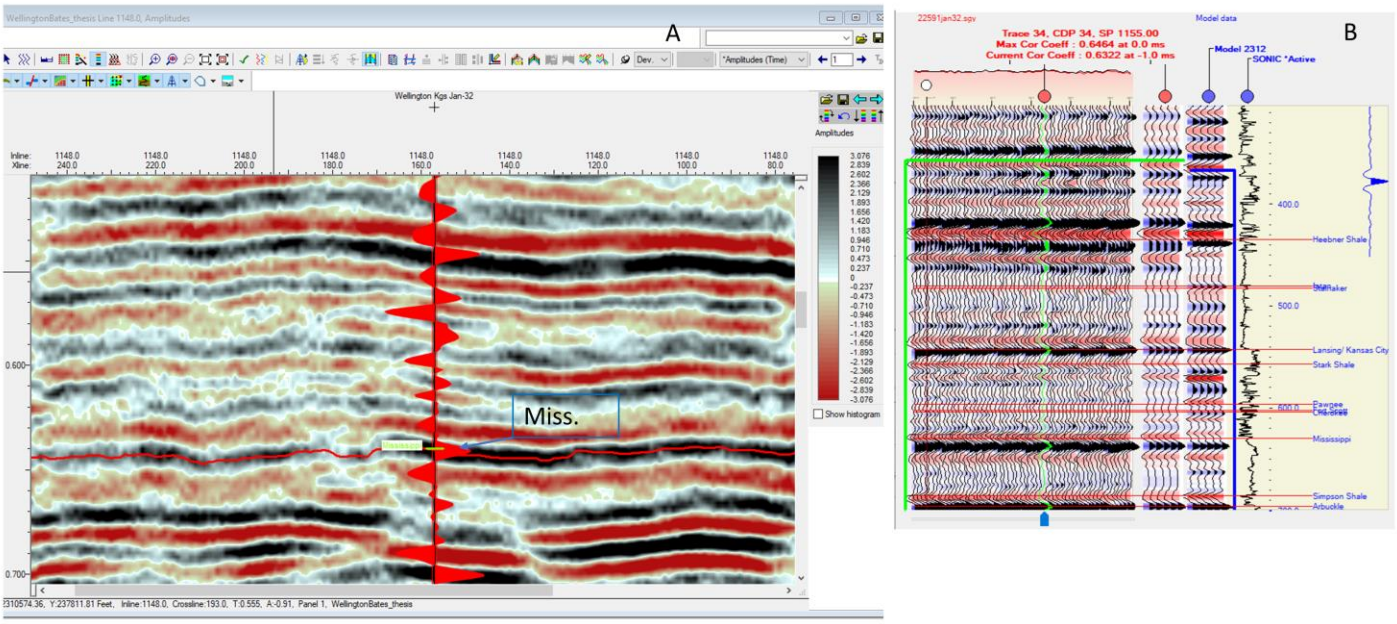

Figure 3.3 (A) The seismic well tie shows the Mississippian peak reflector (blue arrow) and (B) Synthetic 1-D trace model with a correlation coefficient inscribed in red at the top.

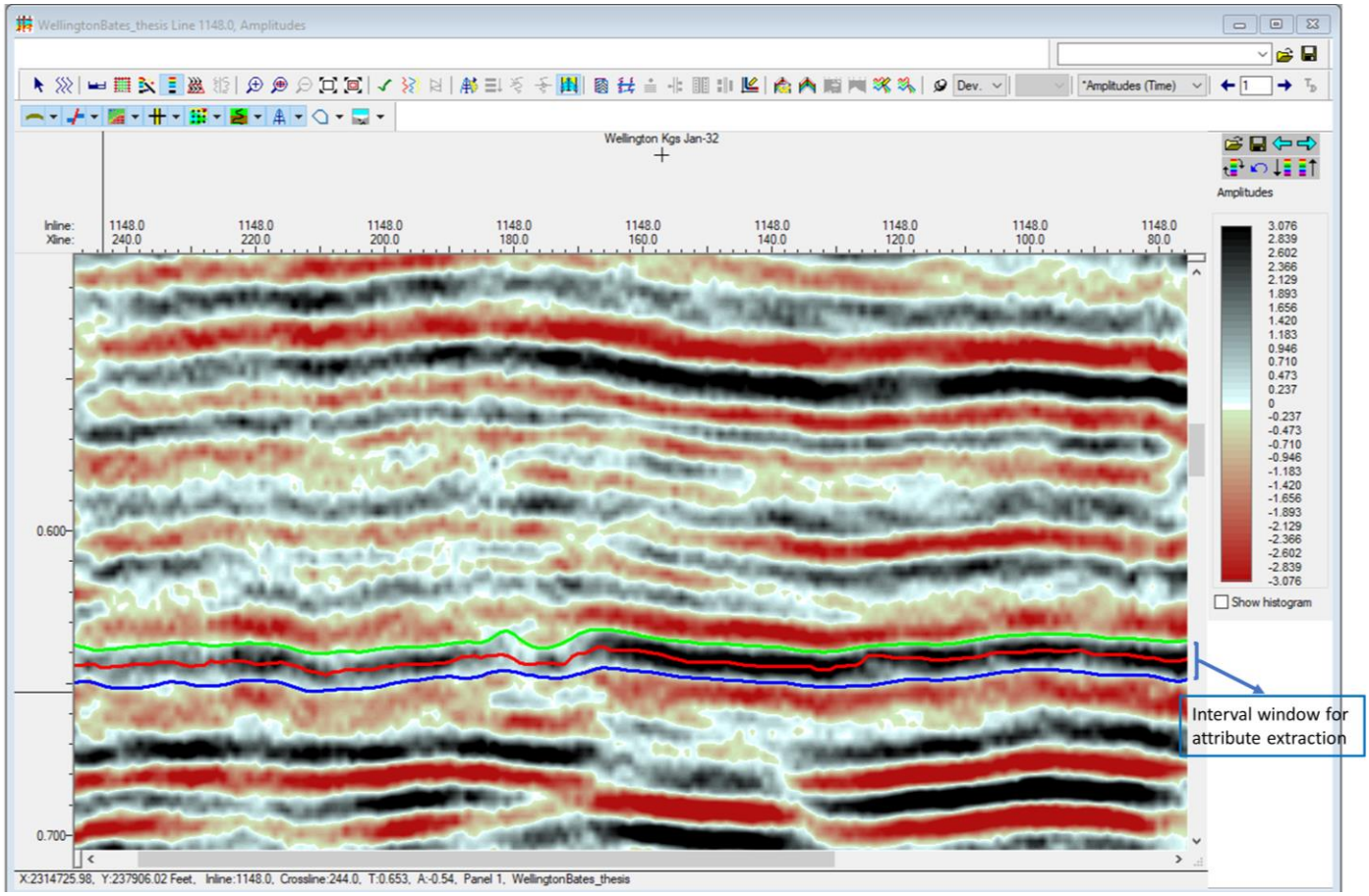

Figure 3.4 Seismic section showing the Mississippian reservoir horizon (red) in the middle peak reflector, the trough-to-peak zero-crossing reflector (green) above, and the peak-to-trough zero-crossing reflector (blue) below forming an interval window for which each seismic attribute was extracted.

Seismic Resolution Enhancement

Spectral whitening processes, such as applying bandpass filters to improve the amplitude spectrum of seismic reflection datasets, are commonly used resolution-improvement techniques. However, they can amplify significant noise (Dowdell et al., 2013; Karsli & Dondurur, 2013). To maximize the resolution of the seismic dataset, spectral whitening was undertaken to obtain amplitude spectrums having close to a flat peak. This intent broadened the original spectrum's frequency bandwidth, increasing resolution. In total, three sets of bandwidth spectral whitening

were applied to the original data, guided by the spectral bandwidth of the original spectrum. The three whitened spectra were evaluated, and that which improved the original's seismic response by reducing the interference effect of thin layer beds was selected for further analysis.

Spectral Decomposition and Seismic Attribute Extraction

Subtle seismic details are often masked in the broad frequency bandwidth of conventional seismic data. The spectral decomposition of the frequency bandwidth into component frequency sub-bands ensures useful, informative frequency sub-bands are utilized to delineate poorly resolved seismic features, and noisy high-frequency sub-bands are discarded. For this study, the original and spectral whitened seismic volumes were decomposed into 20 Hz, 30 Hz, 40 Hz, and 50 Hz sub-bands for post-stack seismic attribute extraction.

Fifteen post-stack seismic attributes encompassing amplitude, waveform, and frequency information were extracted for seismic facies modeling. To eliminate redundancy while capturing maximum variance to delineate subtle variations in seismic facies of the Mississippian reservoir, the attributes were evaluated using a combination of cross-plotting and conventional visualization (see Appendix A). The attribute extraction procedure was a time interval RMS average calculated between the zero-crossing horizon below and above the Mississippian reservoir's peak horizon. This ensured that each attribute calculated for the reservoir captured the entire main reflection lobe. In addition, each attribute was calculated from the original, spectral whitened seismic volumes and their corresponding decomposed sub-bands (Fig. 3.5).

The selected attributes consist of RMS Amplitude, Instantaneous Frequency, Trace Envelope, Bandwidth, Thin Bed Indicator, Normalized Amplitude, Dominant Frequency, Envelope Modulated Phase, Envelope Second Derivative, Envelope Time Derivative,

Instantaneous Frequency Envelope Weighted, Instantaneous Phase, Relative Acoustic Impedance, Wavelet Bandwidth, and Wavelet Dominant Frequency. The attributes extracted were normalized and used as input features for seismic facies machine learning modeling. Software suites used in this study were the IHS Kingdom, Orange Data mining, and Python libraries, including Sci-kit Learn, Seaborn, Pandas, Matplotlib, and NumPy.

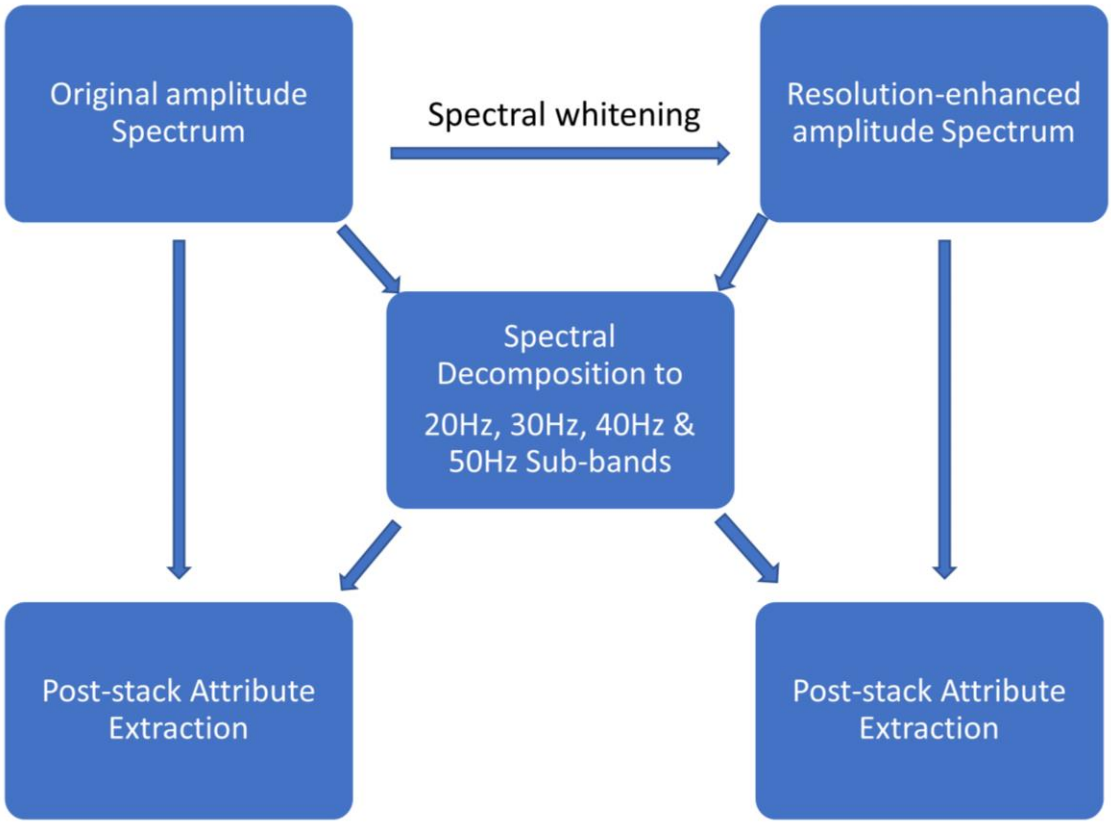

Figure 3.5 Workflow for seismic resolution enhancement and attribute extraction (feature engineering).

Well-log Data

Data

The Gamma Ray log (GR), Neutron Porosity log (NPHI), Density Porosity log (DPHI), Bulk Density log (RHOB), and Photo Electric Factor log (PEF) of four wells penetrating the study area were used for this study. The wells include the Wellington KGS 1-32, 1-28, 2-32, and Bates Unit 4-5. In addition, core log data available for Wellington KGS 1-32 well was also utilized for the study.

Mineral Composition and Reservoir Quality Modeling

With the limitation of core log data for most of the wells in the study area, the best approach to infer lithology variation within the Mississippian reservoir was to calculate Dolomite, Calcite, and Quartz mineral composition from NPHI, DPHI, RHOB, and PEF logs. First, total porosity is calculated by averaging the NPHI and DPHI logs. Next, using weighted equations having total porosity as weights, the apparent grain density (Rhomaa) and volumetric matrix photoelectric absorption (Umaa) were calculated respectively from RHOB and PEF logs. Finally, the composition profile of dolomite, calcite, and quartz (SiO2) was calculated from RHOmaa and Umaa to aid in interpreting seismic facies models.

The study area's reservoir quality grid model was built using variograms and well logs available. The workflow started with establishing a stratigraphic and structural framework using data from 24 wells drilled within the modeling area. Next, the constructed horizons were utilized to generate a single-zone 3D geologic grid with 200`x 200` lateral spacing and 3ft vertical cell thickness. The total number of grid cells was 1,204,612 cells.

Next, facies and log porosity distribution were incorporated into the modeling grid. The facies modeling process involved extracting a facies log from clusters of DPHI and sonic (DT) logs. The resultant facies were upscaled to the grid structure to build a vertical proportion trend. The facies distribution was performed using Sequential Indicator Simulation (SIS) and was conditioned to the facies logs, the vertical proportion curve, and 2D average seismic facies as a lateral trend.

Seismic Facies Modeling

This study utilized two unsupervised machine learning algorithms for seismic facies modeling. One is the agglomerative hierarchical clustering algorithm with Euclidean distance matrix and Ward's linkage parameters. The other is the K-means clustering algorithm with K-means++ centroid initialization and Euclidean distance measure for centroid selection as parameters. The sets of seismic attributes extracted for the Mississippian reservoir horizon were normalized and used as features/inputs for modeling. The workflow developed in this study was to enable some evaluations to be made; one was to establish cluster consistency between the two algorithms as ground truth to delineate inherent clusters in the data, and the other was to evaluate the effect of resolution enhancement (spectral whitening) in clustering (Fig. 3.6). To assess cluster consistency, hierarchical and K-means clusters were built using attributes extracted at total frequency bandwidth before and after resolution enhancement, individual sub-bands 20 to 50 Hz before and after resolution enhancement, and composite 20-50 Hz sub-bands before and after resolution enhancement. In addition, k-means clusters for the attribute sets were used to evaluate resolution enhancement.

Finally, an interpreter's seismic facies model was developed by integrating cluster facies models, petrophysical models from well logs, and domain knowledge of the geometry of carbonate depositional systems.

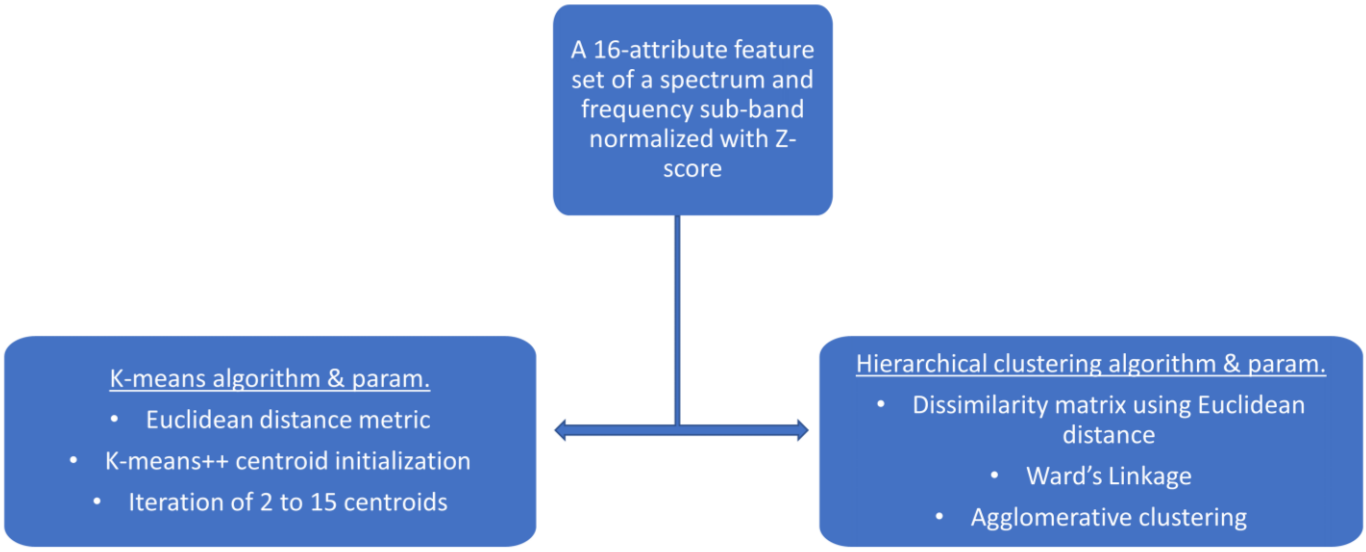

Figure 3.6 Workflow for seismic facies clustering (machine learning modeling).

Chapter 4 - Results and Discussion

Spectral Whitening

The original frequency bandwidth of the seismic data (spectrum 1) was 25 Hz to 60 Hz. The three enhanced amplitude spectrums obtained by spectral whitening had frequency bandwidths of 10 Hz to 80 Hz (spectrum 2), 30 Hz to 110 Hz (spectrum 3), and 20 Hz to 125 Hz (spectrum 4) (Fig. 4.1). All three enhanced spectrums had broad frequency bandwidths that fit within the amplitude spectrum of the original seismic data; however, spectrum 4 was selected as the enhanced amplitude spectrum upon seismic section evaluations proved it illuminated to a greater detail a pinch-out feature formed by peak reflectors at about 0.44s two-way time (TWT) (Fig. 4.2). Notwithstanding, the improved resolution, especially at low-frequency bandwidth which is essential for reducing the thin bed interference within the Mississippian carbonate reservoir located at about 0.64s TWT, caution against the amplification of high-frequency noise is taken by subsequently assessing frequency sub-bands to select optimum ones through spectral decomposition.

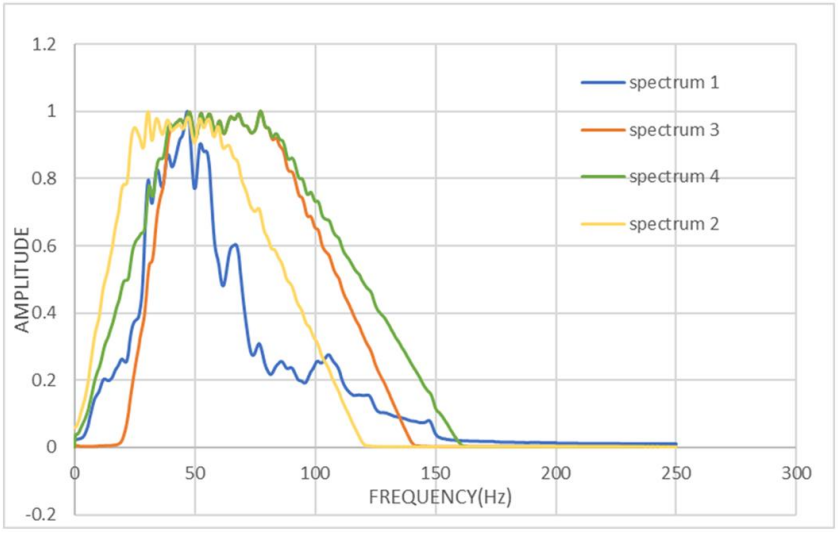

Figure 4.1 Plot showing frequency bandwidths of the original amplitude spectrum 1(blue), spectral whitened amplitude spectrum 2(yellow), 3(orange), and 4(green).

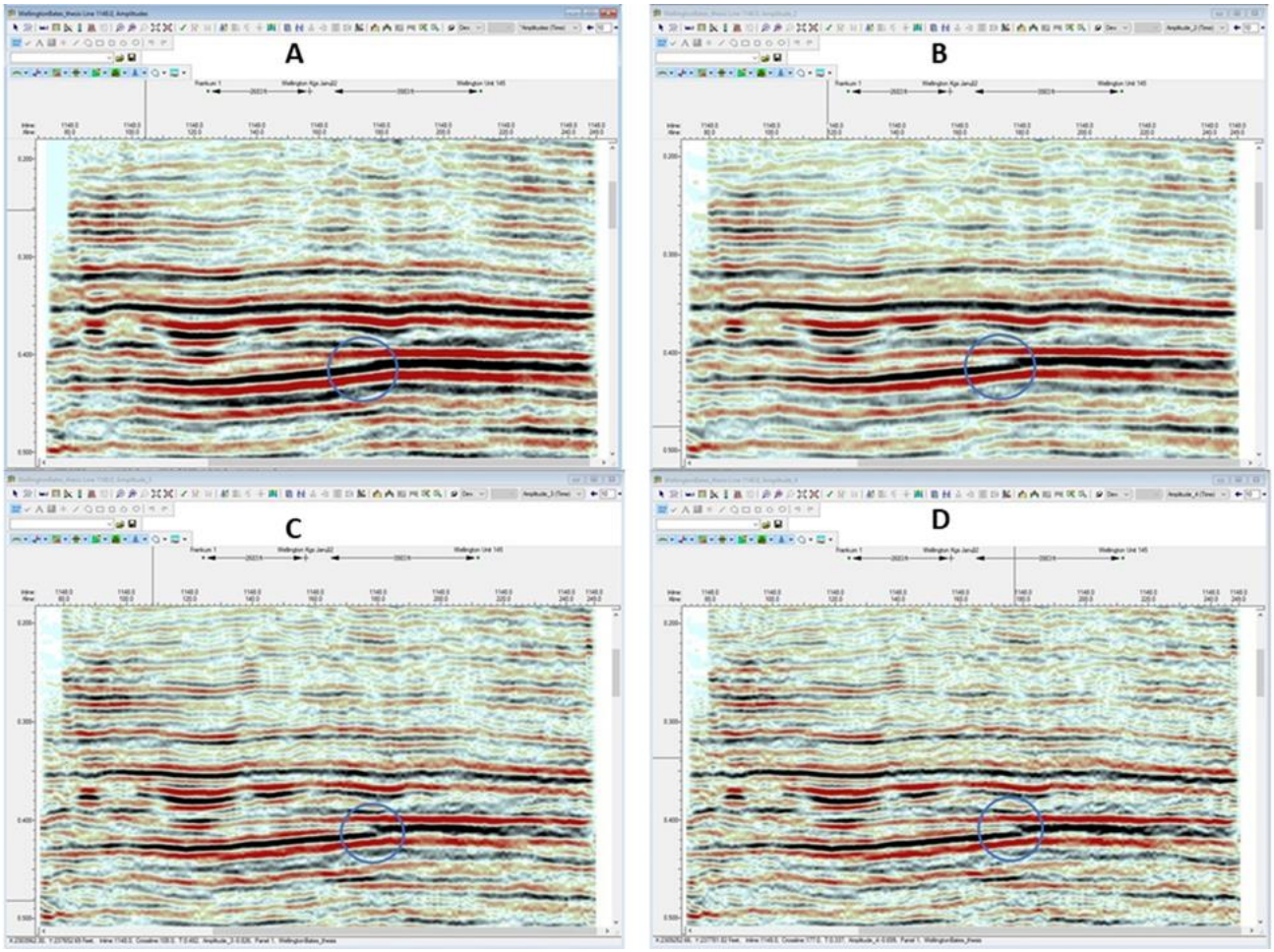

Figure 4.2 Seismic sections for the respective amplitude spectrums. The blue circle highlights a pinch-out feature progressively resolved due to the reduction in interference of thin beds as frequency bandwidth increases from the original spectrum(A) to spectrum 4(D).

Mineral Composition and Reservoir Quality

Dolomite, Quartz, and Calcite mineral composition variability within the Mississippian reservoir were calculated from Wellington KGS 1-32, 2-32, 1-28 wells in the Wellington field and Bates Unit 4-5 well in the Anson-Bates field of the study area (Fig. 4.3). Reservoir quality variability with classes good, moderate, poor and tight/shale were modeled for the same reservoir from the same wells in the Wellington field of the study area along a profile line ‘A-A1’ (Fig. 4.4). The Bates Unit 4-5 well (Fig 4.3a) shows averagely high calcite mineral, followed by dolomite and quartz indicative of low dolomitization and silicification diagenesis.

For the Wellington field wells, on average, the KGS 1-32 well (Fig. 4.3c) has the highest dolomite and quartz mineral content with the minor calcite mineral, followed by the KGS 1-28 well (Fig. 4.3d), edging slightly over KGS 2-32 well (Fig. 4.3b) indicative of extensive dolomitization and silicification in this order. Correlating the mineral concentration of the wells penetrating the Mississippian carbonate reservoir in the Wellington field with the reservoir quality profile line 'A-A1' (Fig. 4.4) shows high average dolomite and quartz content result in good average reservoir quality. This reaffirms the assertion by Watney et al. (2001) that the petrophysical properties of the Mississippian 'chat' reservoirs are altered or controlled by dolomitization and silicification. The inferences drawn from the mineral composition and reservoir quality of the limited wells in the study area helped understand the seismic facies subsequently delineated through clustering.

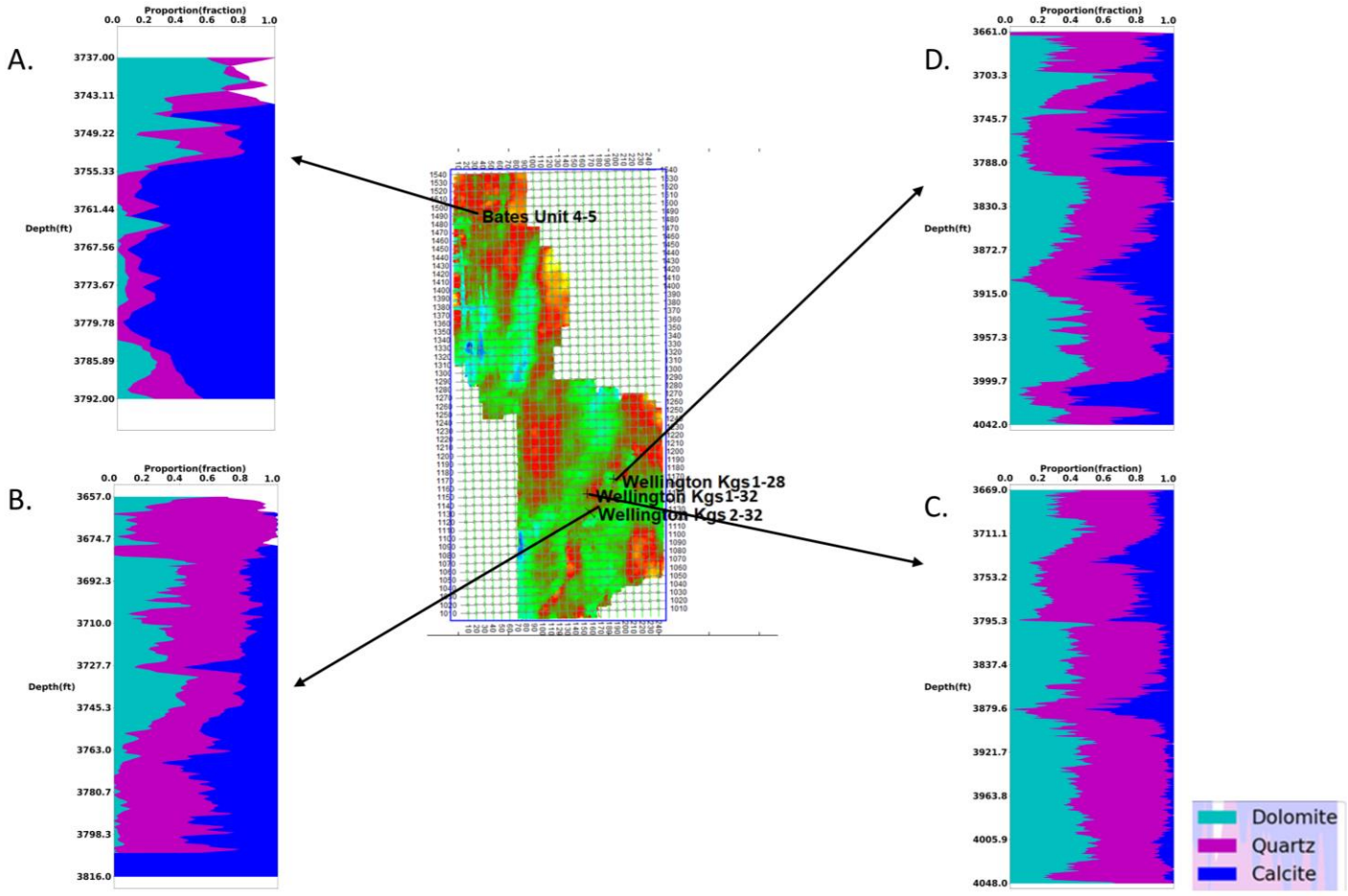

Figure 4.3 Dolomite, Quartz, and Calcite mineral proportions for selected wells within the Anson-Bates and Wellington field part of the study area.

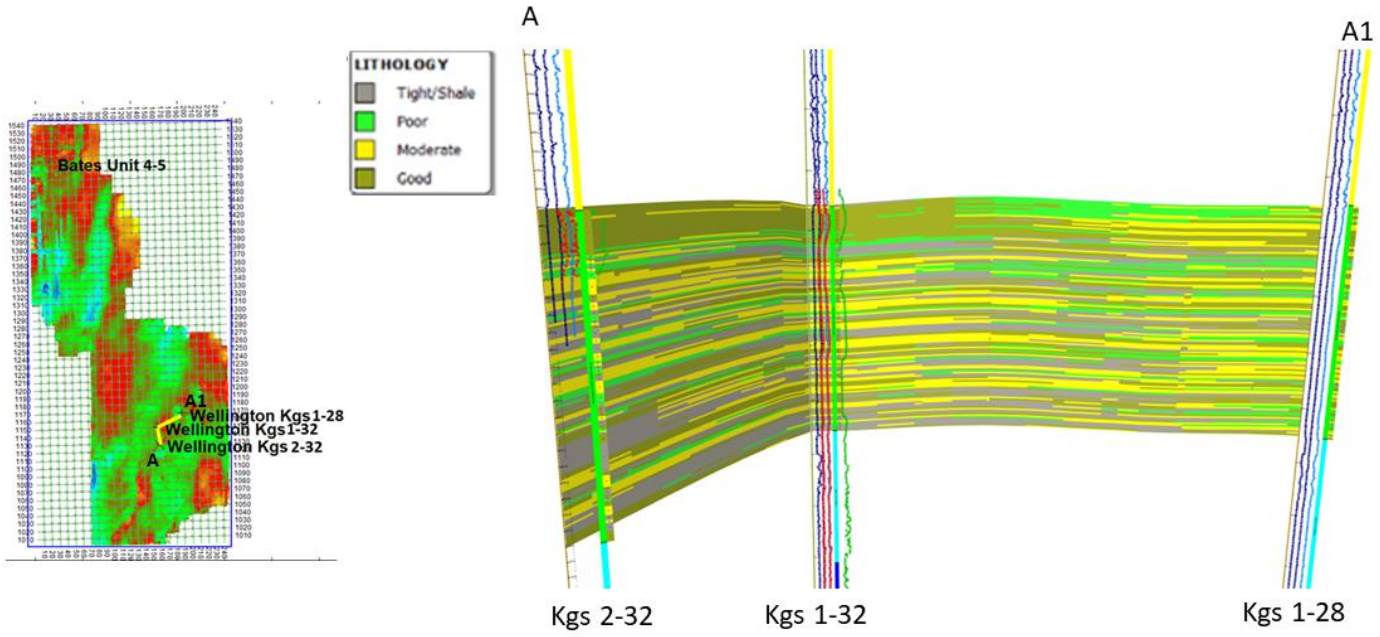

Figure 4.4 Grid model showing the variability of reservoir quality within the Wellington field part of the study area across the cross-section line A-A1.

Seismic Facies Analysis

Consistency of Seismic Facies with Clustering

This study leveraged the consistency of clusters between the K-means and hierarchical clustering algorithms as a first-hand validation of inherent clusters (seismic facies) in the seismic data coupled with spatial continuity of clusters for each feature set to select the optimum number of clusters with geological plausibility. The K-means++ centroid initialization used in the K-means algorithm with an iteration of 2 to 15 centroids and silhouette score calculated for each set of centroids in the loop eliminated the bias of randomly selecting the k-number of centroids. In contrast, Ward's linkage used in the agglomerative hierarchical clustering algorithm ensured clusters formed at each node or hierarchy best reduced the intra-cluster variance, hence, the resulting total variance within the data set. For each spectrum and frequency sub-band, it was

observed that both algorithms produced the least noisy clusters with minimal variations for a specific number of clusters (Fig. 4.5 to 4.10).

Comparatively, the K-means cluster distribution highlighted finer spatial or lateral partitions for the same feature set and cluster number. This justified some researchers' recommendation of using hierarchical clustering to identify initial seed points or 'k' centroids in k-means clustering with random centroid initialization (Murtagh & Legendre, 2014; Wang, 2012). As a result, the K-means algorithm was selected to evaluate the effect of resolution enhancement on seismic facies delineation.

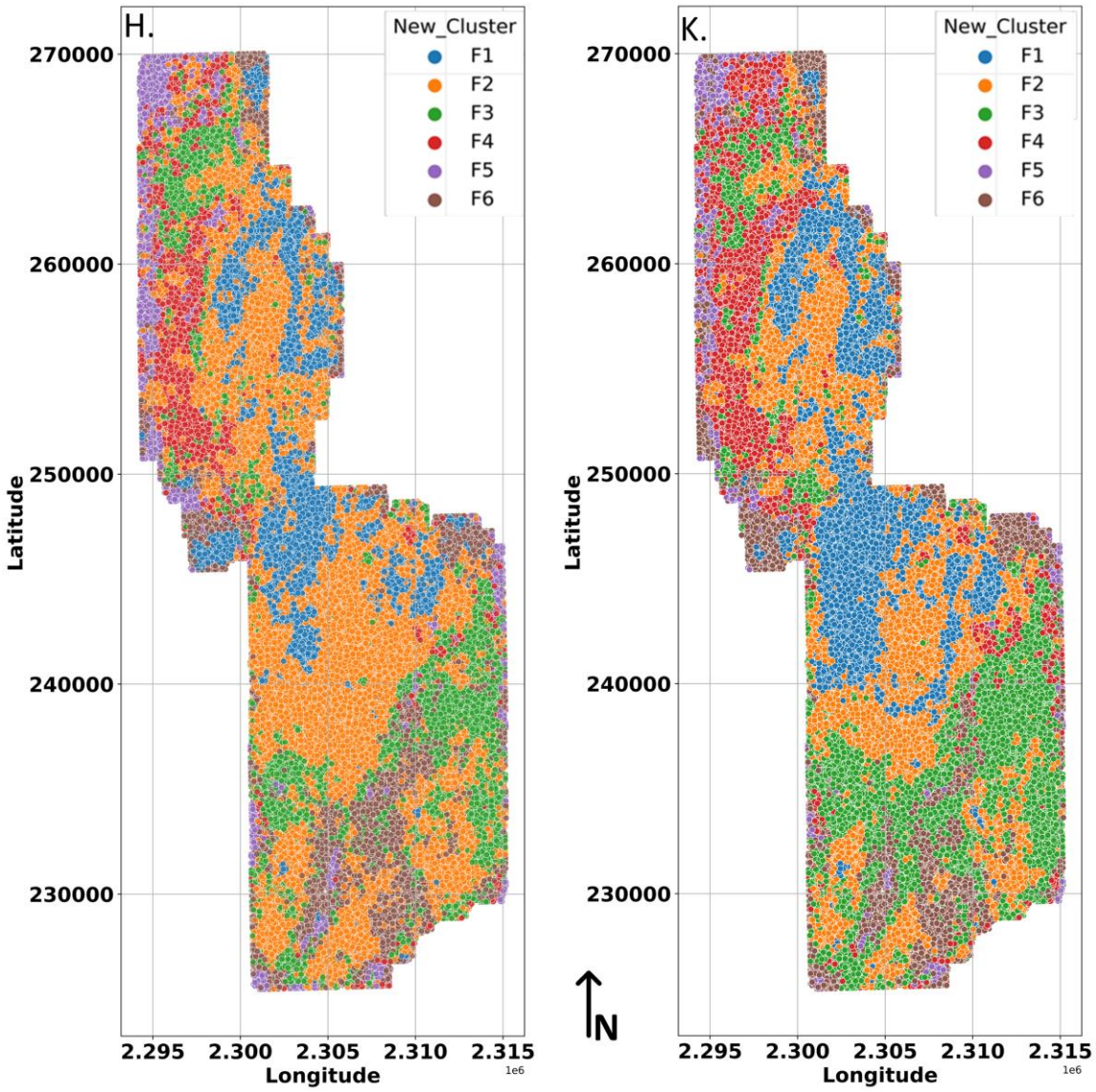

Figure 4.5 Delineated seismic facies by hierarchical (H) and K-means (K) clustering for feature sets extracted from the original spectrum of the data.

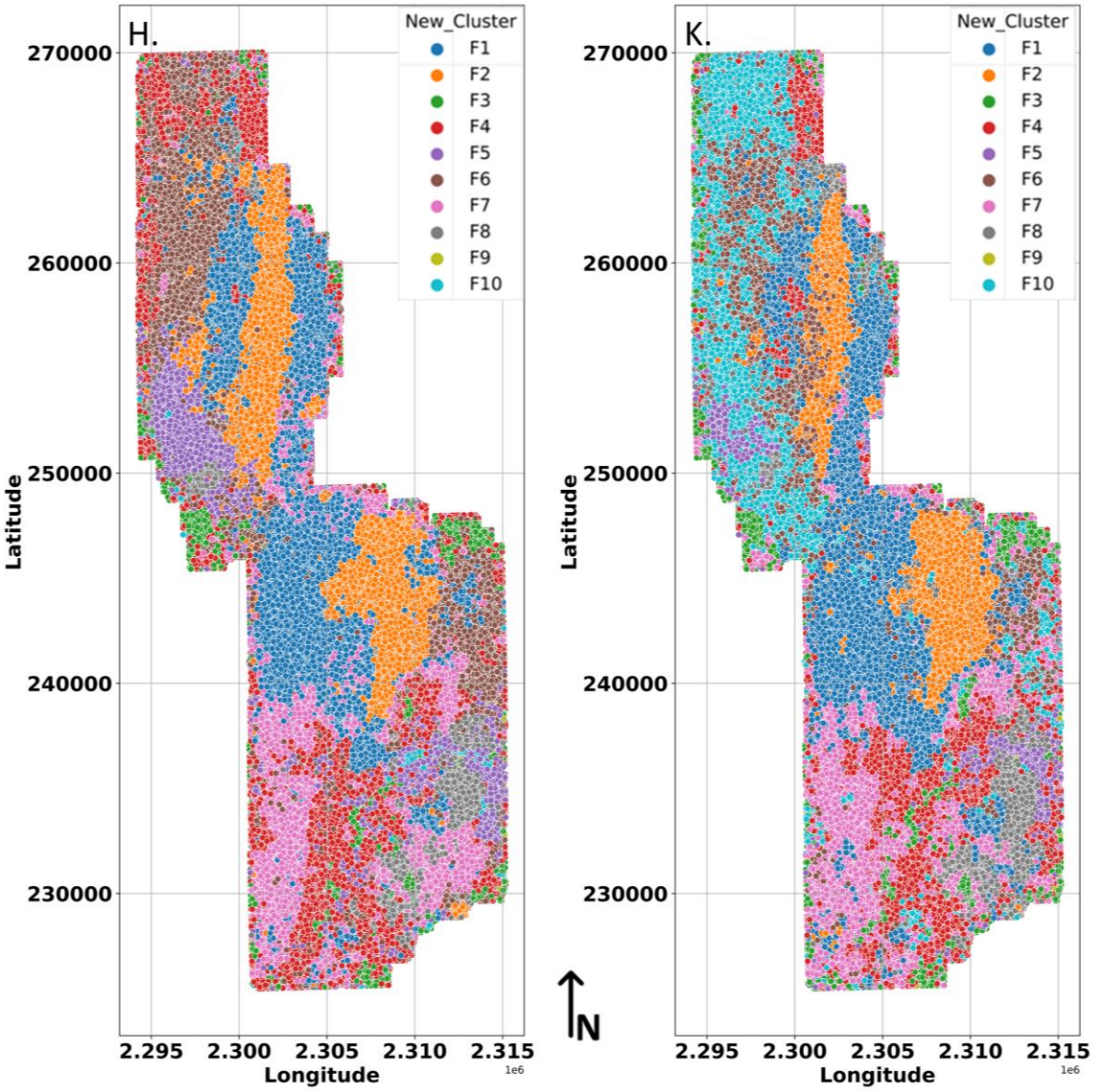

Figure 4.6 Delineated seismic facies by hierarchical (H) and K-means (K) clustering for feature set extracted from the original spectrum at 20 Hz frequency sub-band of the data.

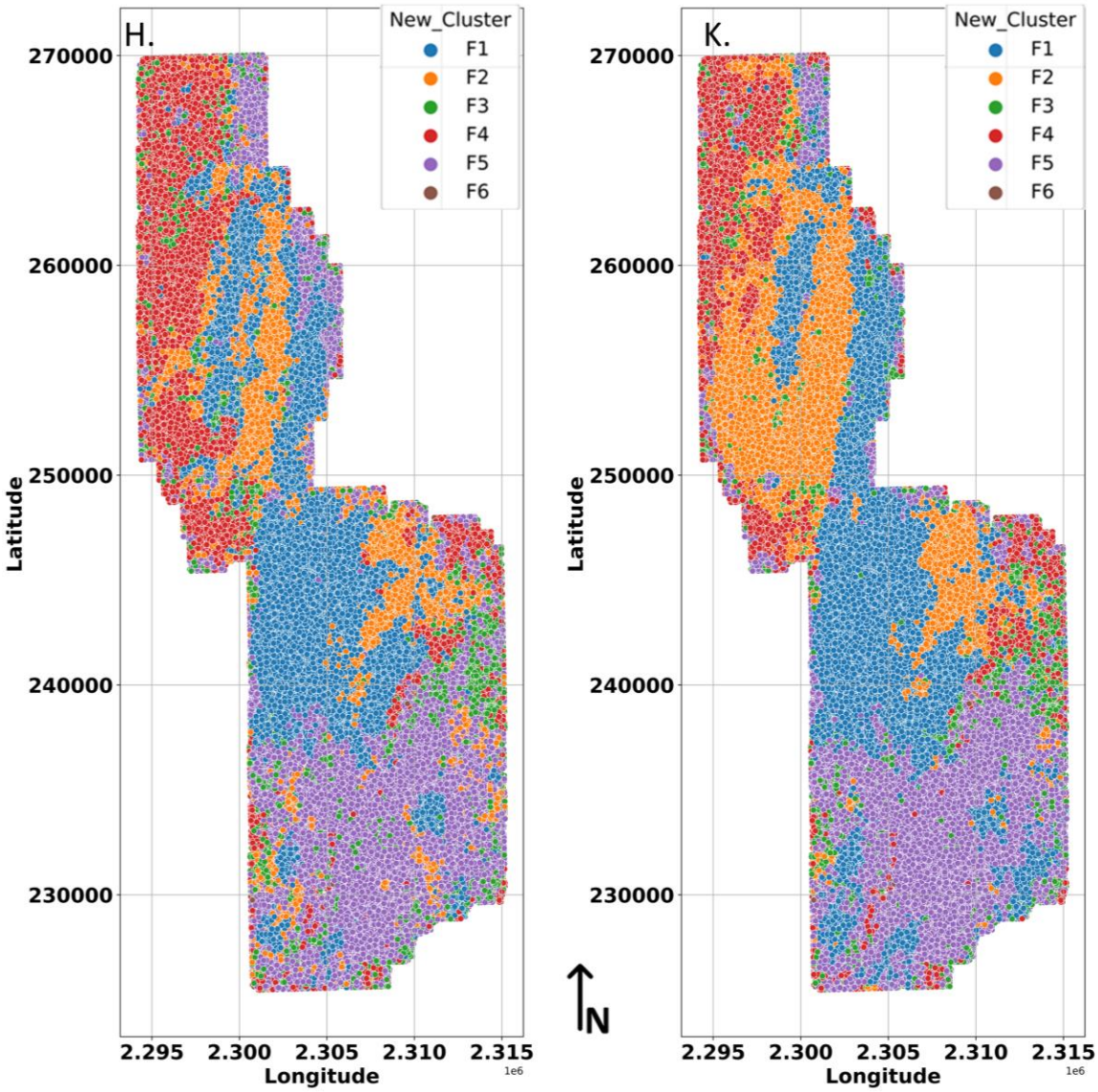

Figure 4.7 Delineated seismic facies by hierarchical (H) and K-means (K) clustering for feature set extracted from the original spectrum at 30 Hz frequency sub-band of the data.

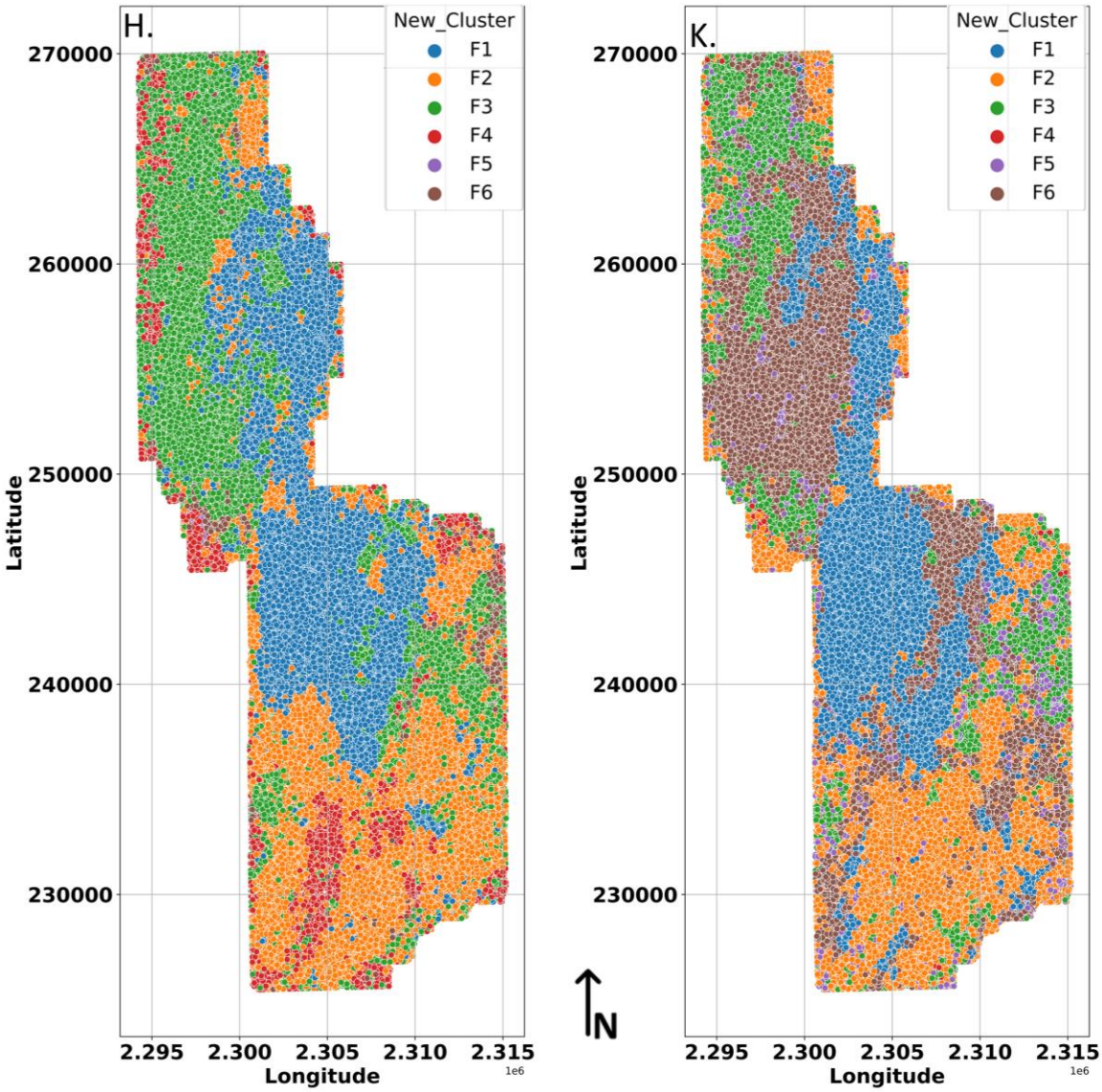

Figure 4.8 Delineated seismic facies by hierarchical (H) and K-means (K) clustering for feature set extracted from the original spectrum at 40 Hz frequency sub-band of the data.

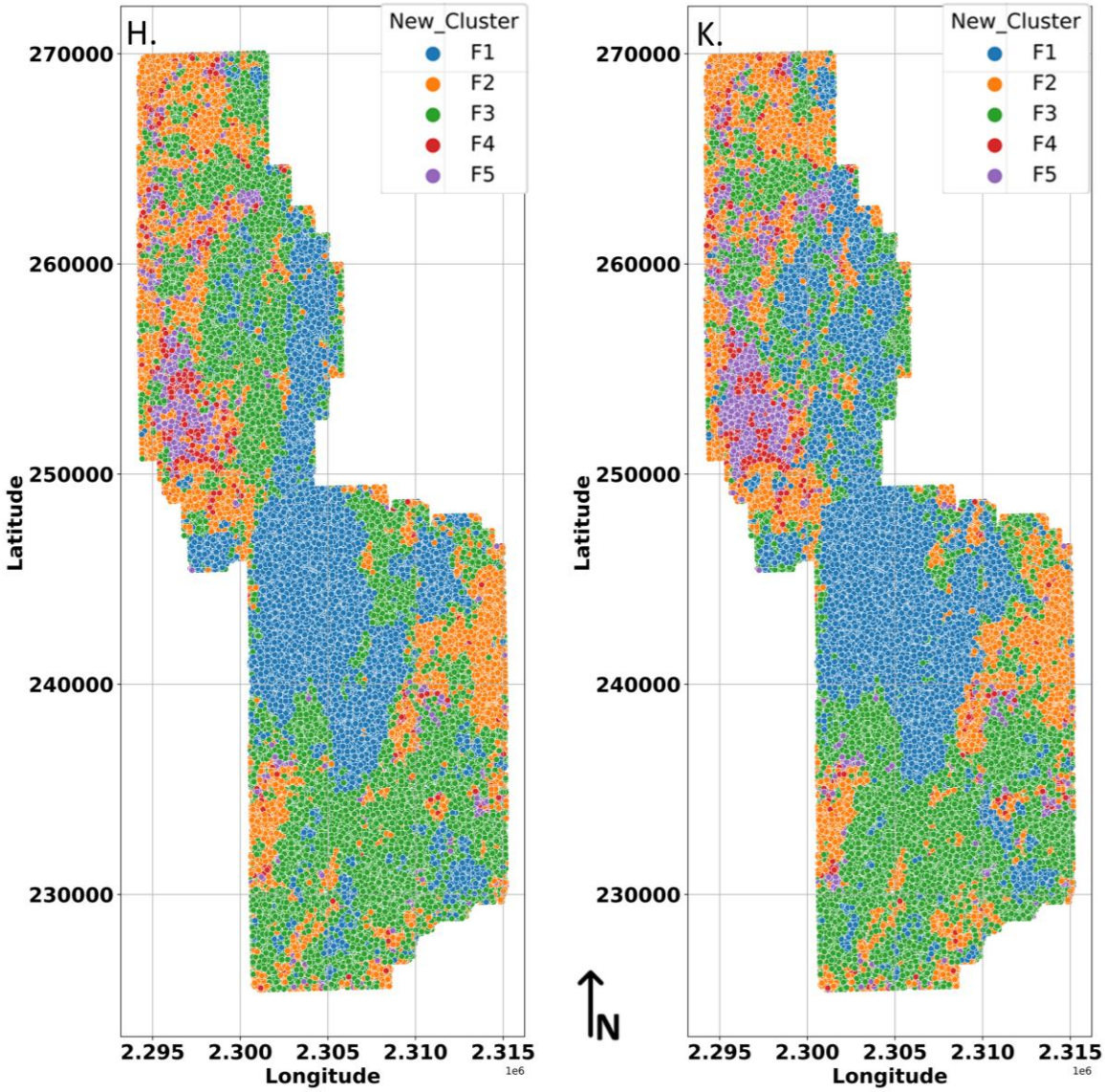

Figure 4.9 Delineated seismic facies by hierarchical (H) and K-means (K) clustering for feature set extracted from the original spectrum at 50 Hz frequency sub-band of the data.

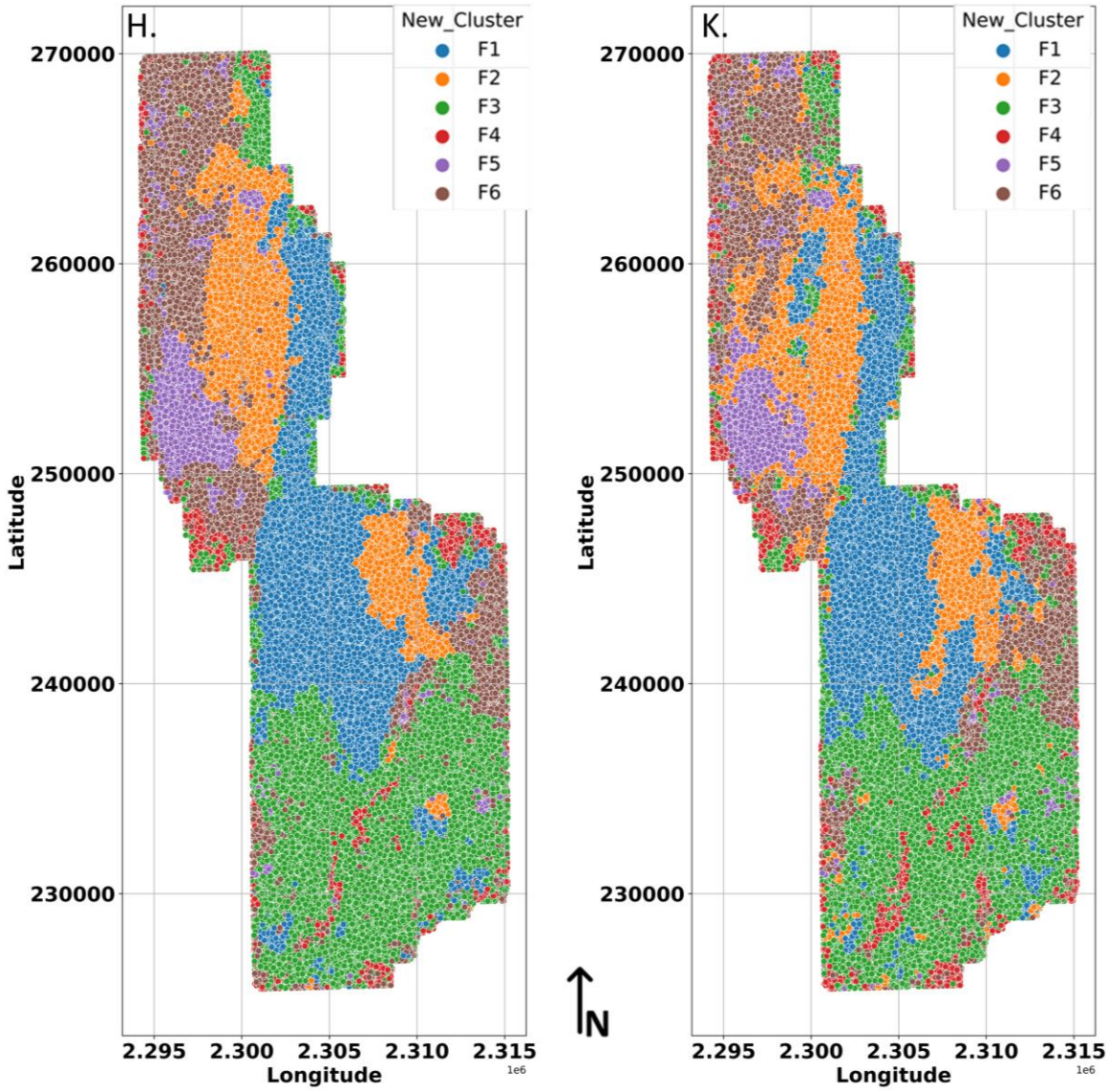

Figure 4.10 Delineated seismic facies by hierarchical (H) and K-means (K) clustering for feature set extracted from the original spectrum at composite 20 Hz to 50 Hz frequency sub-band of the data.

Resolution Enhancement Techniques on Seismic Facies (Clusters)

Evaluating the effect of resolution enhancement techniques applied to the original data, only seismic facies (clusters) with geological plausibility were considered. Acknowledging the fact that spectral whitening improves low-frequency resolution but amplifies high-frequency noise as seismic artifacts into the data, spectral decomposition was also employed to ensure

noisy high-frequency sub-bands are eliminated. Therefore, the final interpreter's seismic facies model was evaluated based on spatial integrity and continuity of clusters and how they fit into the conceptual carbonate shelf/ramp depositional setting of the study area as well as how the cluster spatial distributions fit into the existing concepts of diagenesis and petrophysical models developed by earlier researchers (Ohl & Raef, 2014; Watney et al., 2001; Wilson et al., 2019).

For features extracted from the entire frequency bandwidth, the delineated facies(clusters) increased from six for the original amplitude spectrum to seven for the resolution-enhanced spectrum (Fig. 4.11). For features extracted at 20 Hz frequency sub-band, ten facies were delineated for the original and resolution-enhanced amplitude spectrums with a difference in the spatial distribution of some delineated facies within the study area (Fig. 4.12). For features extracted at 30 Hz, 40 Hz, and 50 Hz sub-bands, a single difference in the number of facies delineated was observed between the original and resolution-enhanced spectrum (Fig. 4.13 to 4.15). Further, using a composite feature set extracted for 20 Hz to 50 Hz frequency sub-bands also resulted in a single difference in the number of facies between the original and resolution-enhanced spectrum (Fig. 4.16).

Finally, deductions drawn from the resolution enhancement techniques were; (1) the frequency sub-bands 20 Hz to 50Hz contained optimum signal-to-noise data to characterize facies variability in the Mississippian reservoir at the study area, (2) fusing the feature set extracted at 20 Hz to 50Hz sub-bands as composite feature set produced a finer spatial distribution of seismic facies by masking out random noises dominant at each frequency sub-band (Fig. 4.17b) and, (3) the composite 20 Hz to 50 Hz feature set extracted from the spectral whitened amplitude spectrum resolved thin/subtle facies masked in the original spectrum (Fig.

4.17c). Hence, the facies model built with the resolution-enhanced spectrum was selected as a base for the interpreter's seismic facies model (Fig. 4.17c).

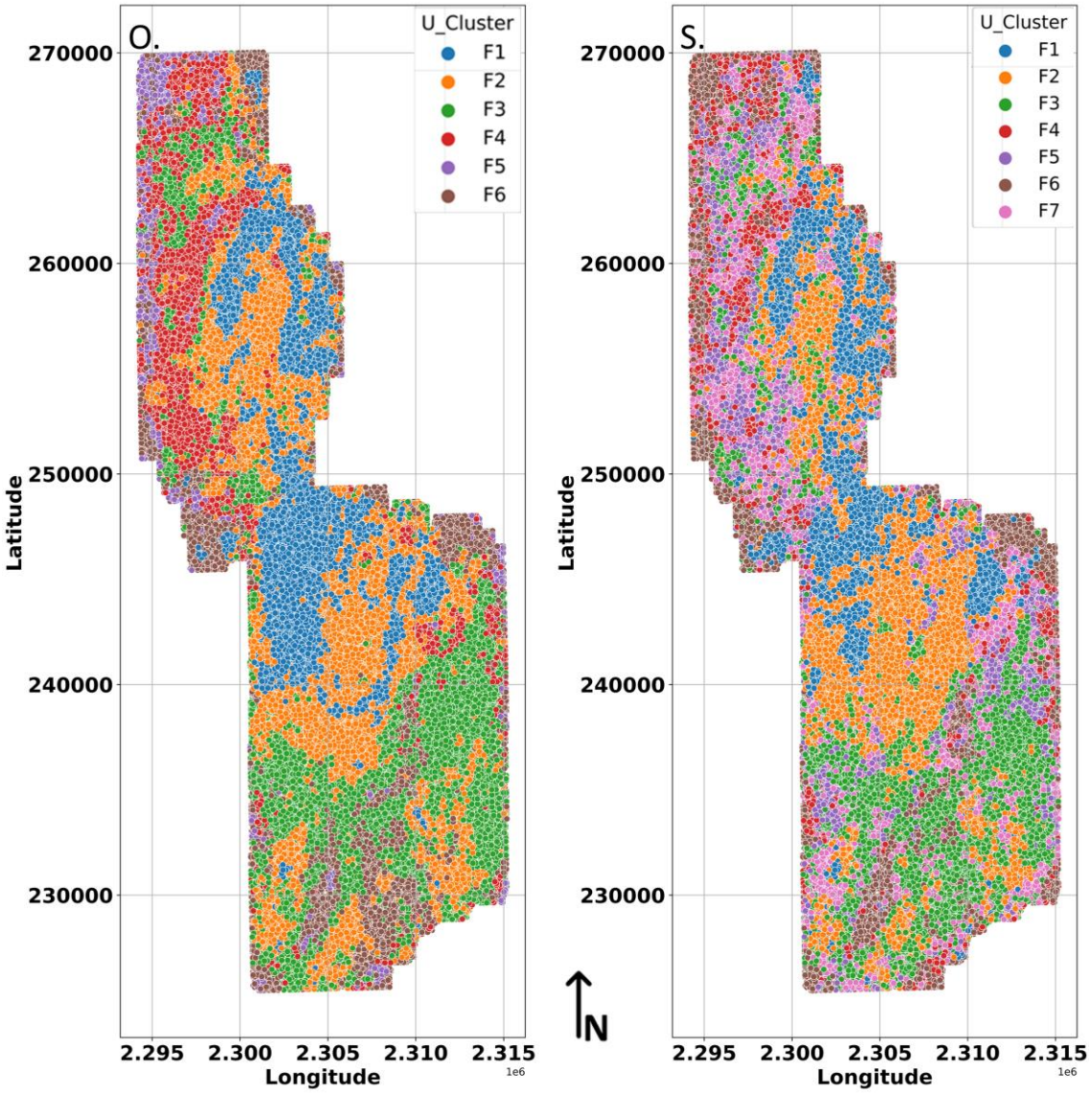

Figure 4.11 Delineated seismic facies from original (O) and resolution-enhanced (S) spectrums at the entire frequency bandwidth of the data.

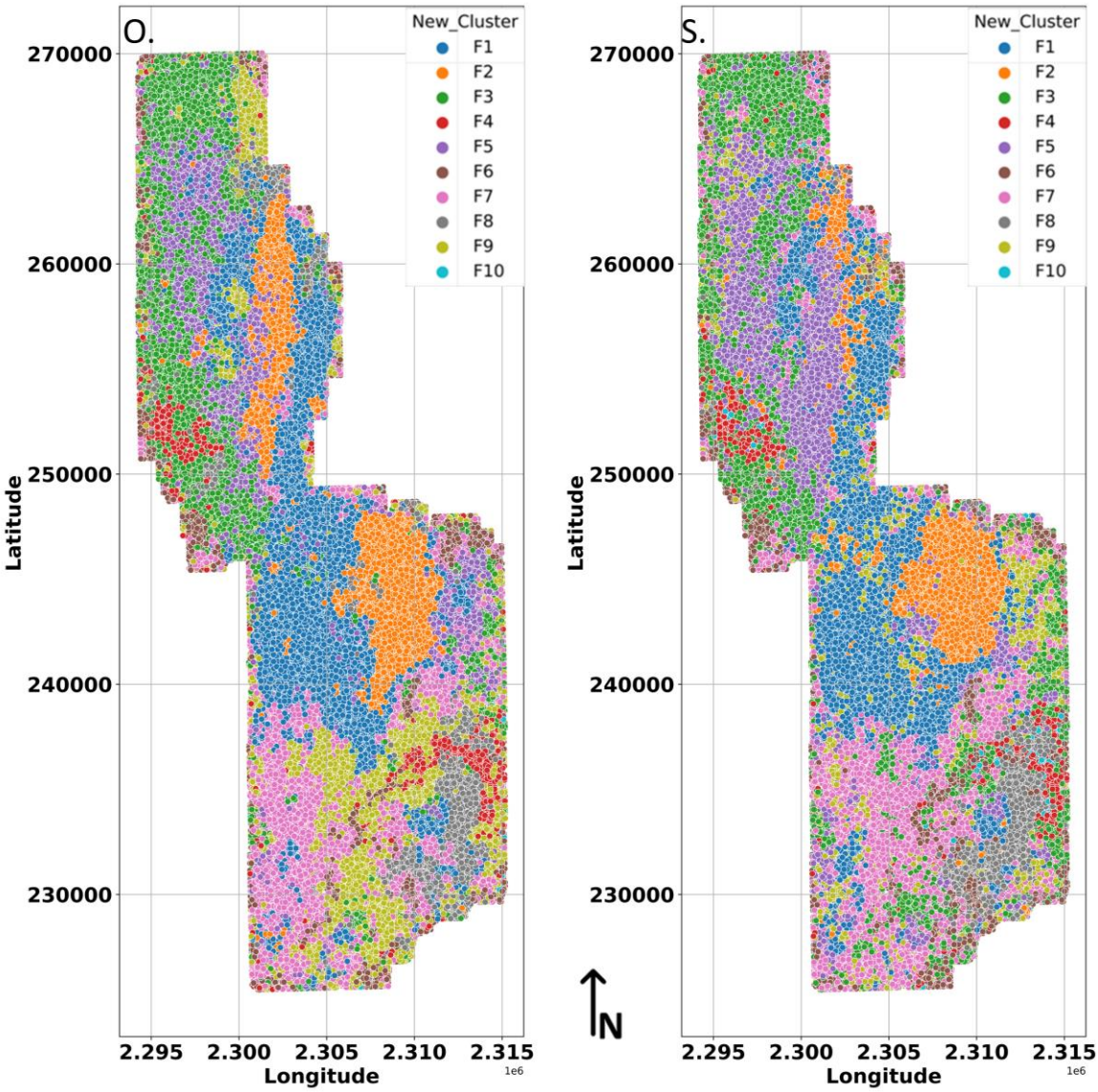

Figure 4.12 Delineated seismic facies from original (O) and resolution-enhanced (S) spectrums at 20 Hz frequency Sub-band of the data.

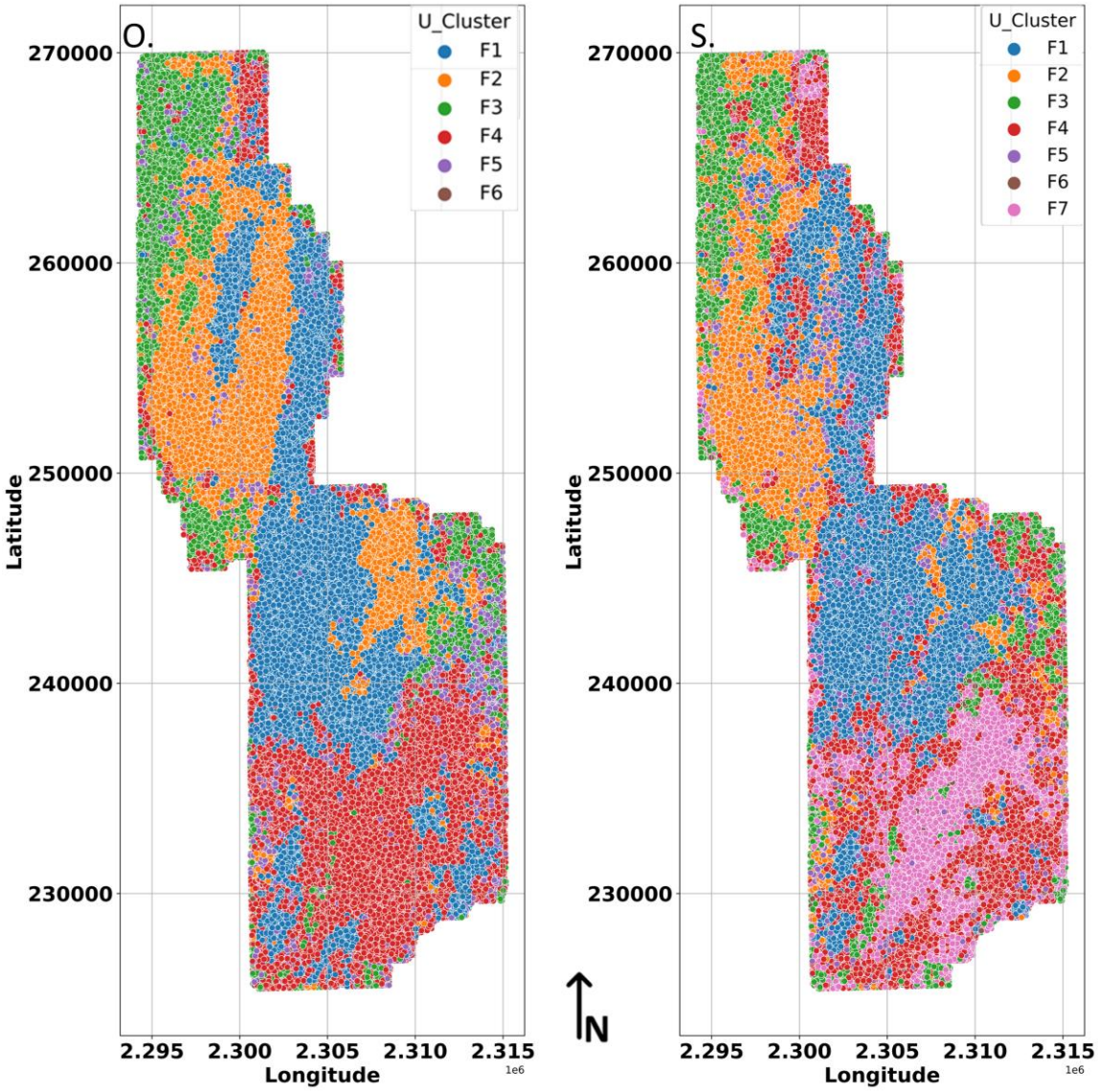

Figure 4.13 Delineated seismic facies from original (O) and resolution-enhanced (S) spectrums at 30 Hz frequency Sub-band of the data.

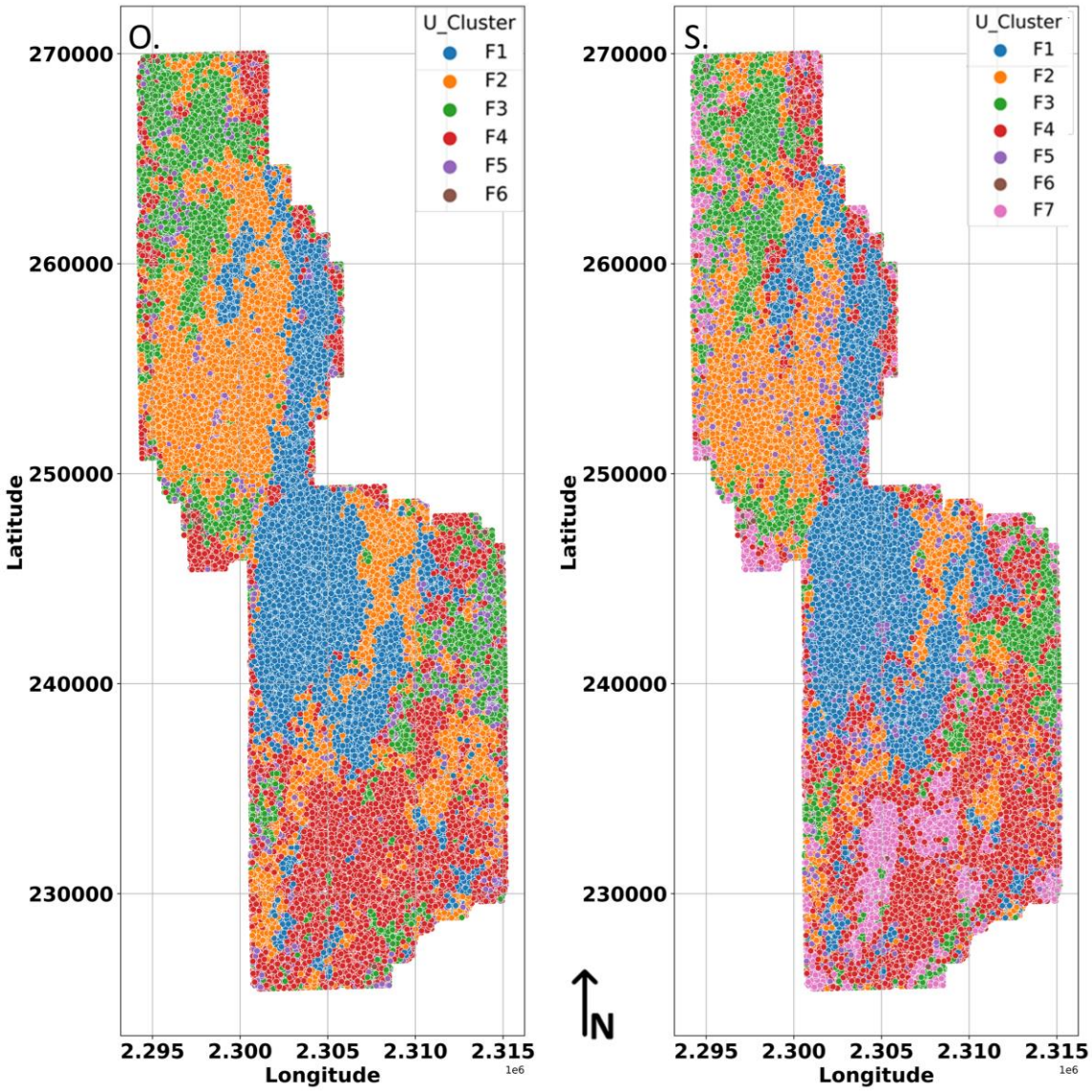

Figure 4.14 Delineated seismic facies from original (O) and resolution-enhanced (S) spectrums at 40 Hz frequency Sub-band of the data.

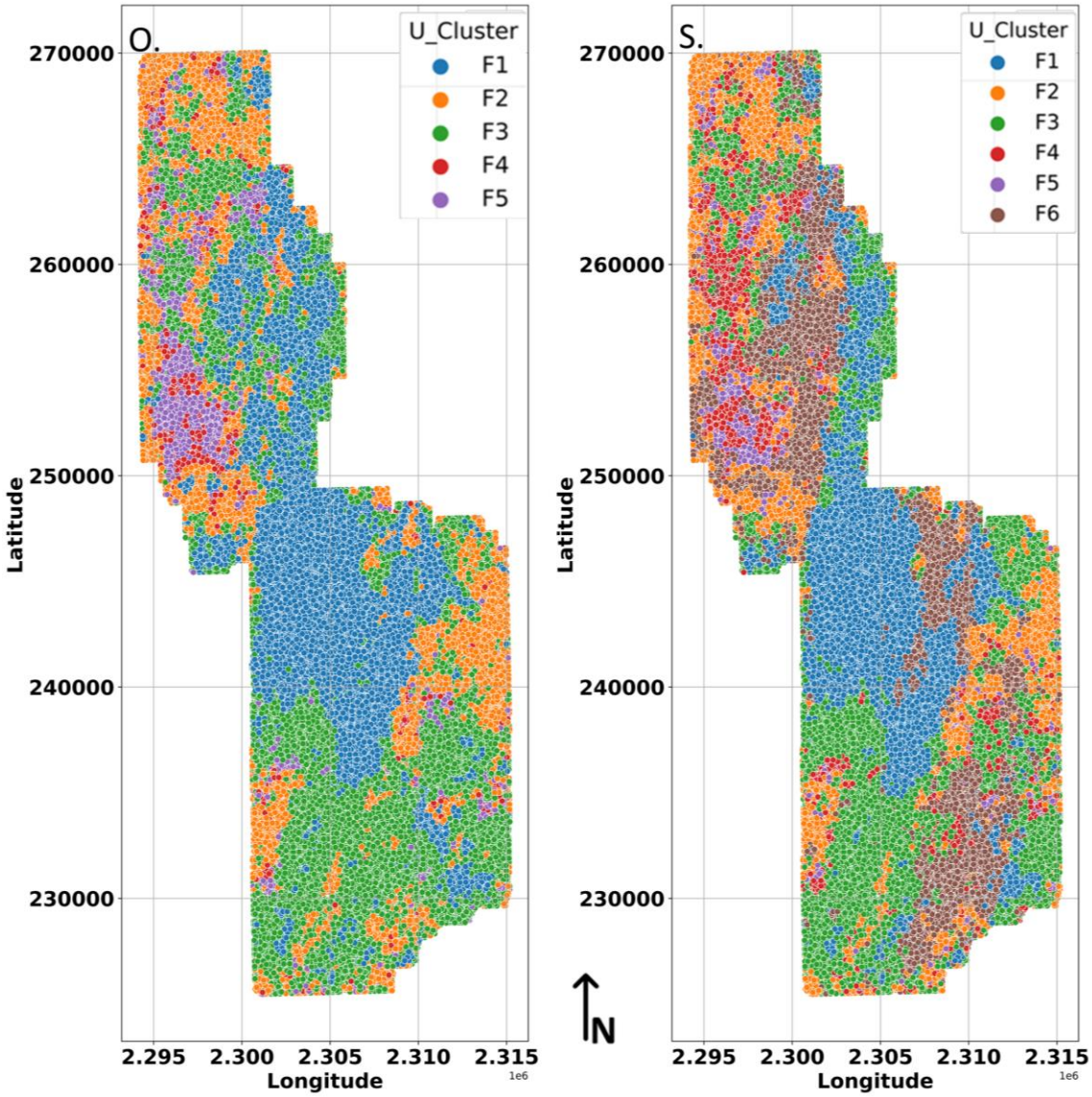

Figure 4.15 Delineated seismic facies from original (O) and resolution-enhanced (S) spectrums at 50 Hz frequency Sub-band of the data.

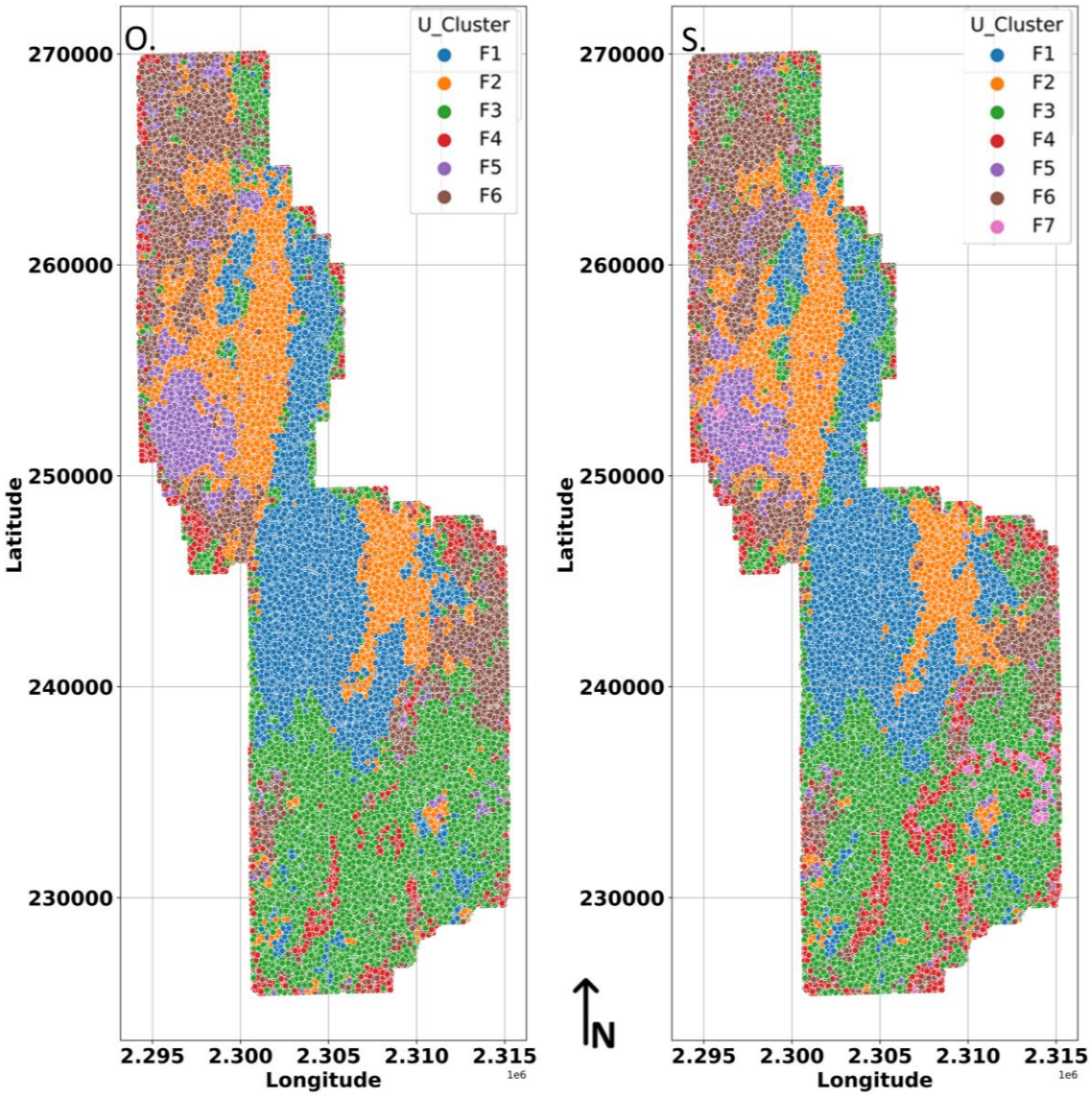

Figure 4.16 Delineated seismic facies from original (O) and resolution-enhanced (S) spectrums at composite 20 Hz to 50 Hz frequency Sub-band of the data.

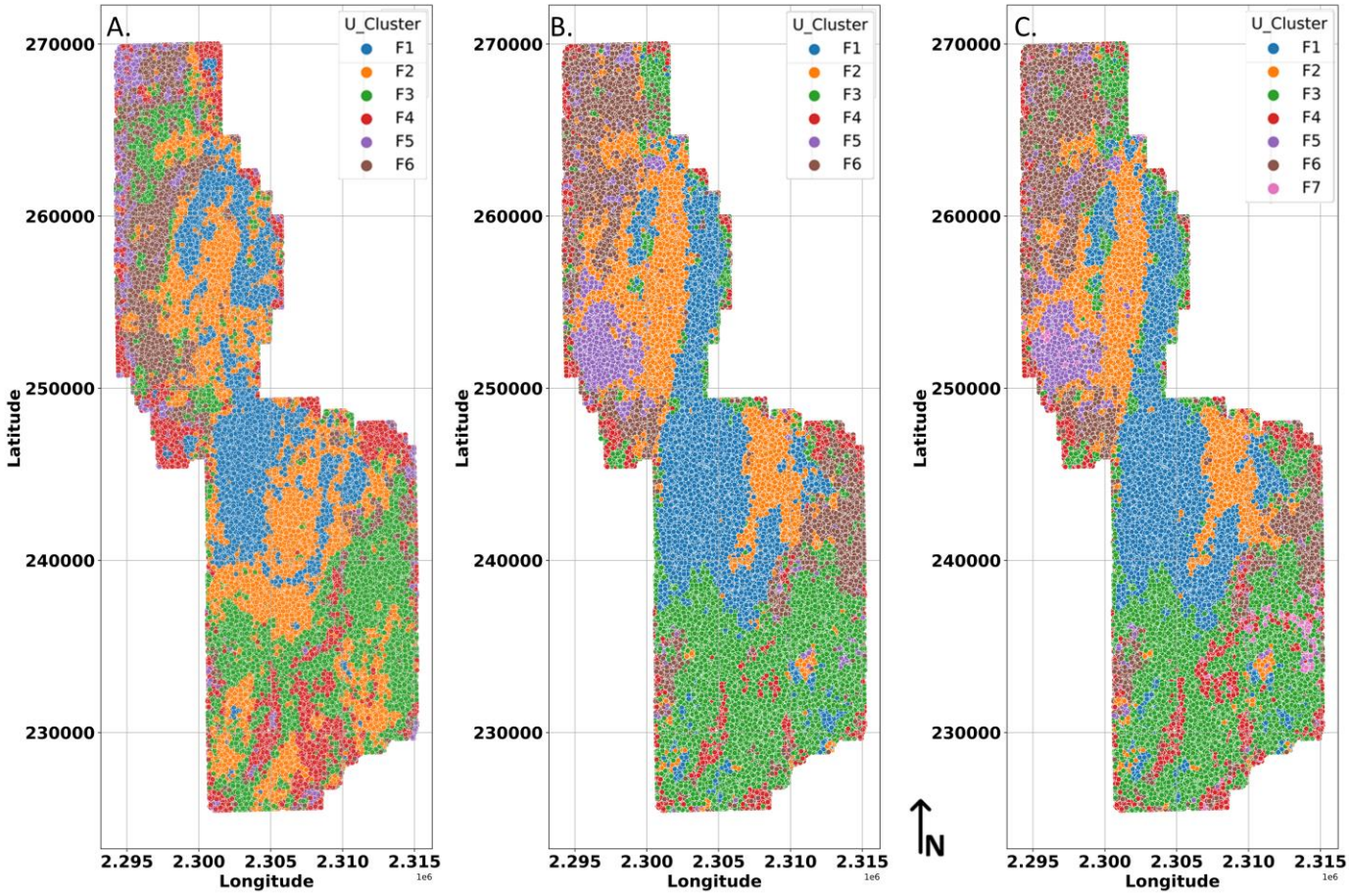

Figure 4.17 Seismic facies maps at (A) total frequency bandwidth of original spectrum, (B) composite 20 Hz to 50 Hz frequency sub-bands of the original spectrum, and (C) composite 20 Hz to 50 Hz of the spectral whitened spectrum.

Interpreter's Seismic Facies Model

Integrating the facies map (Fig. 4.17c), the mineral proportions for available wells in the study area (Fig. 4.3), the reservoir quality model for available wells (Fig. 4.4), the petrophysical (porosity) facies model built by Ohl & Raef (2014) (Fig. 4.18a), and the distance matrix for the centroids of seismic facies (Fig. 4.18c) brought to bear these details;

• A discernable boundary (marked by a black dashed line in figure 4.18b) in the Wellington field of the study area resolved to be the shelf edge marking the transition from the carbonate (Burlington) shelf facies (region above the black line in figure 4.18b) to the shelf

margin facies (region below the black line in figure 4.18b). This inference is also affirmed by the location of the study area on the paleo-depositional model of the midcontinent portion of the Early Mississippian (Fig. 2.1) (Wilson et al., 2019).

• From figure 4.3, well KGS 1-32 (c) has the highest combined dolomite and quartz average composition and penetrates facies F1 within the shelf region (Fig. 4.18b). KGS 1-28 well (d) follows and penetrates facies F6 within the shelf margin region (Fig. 4.18b). KGS 2-32 well (b) is next and penetrates facies F3 within the shelf margin region (Fig. 4.18b). Lastly, Bates Unit 4-5 (a) also penetrates facies F3 within the shelf region (Fig. 4.18b). Correlating these with the petrophysical facies model in figure 4.18a revealed facies F1 maps to high porosity facies (Class 1) with an average porosity greater than 12%. Facies F3 and F6 map to low porosity facies (Class 3) with an average porosity of less than 8%. However, assessing from the distance matrix in figure 4.18c, facies F3 and F6 are closer in comparison to the other facies coupled with the fact that the well penetrations in these two facies proved F6 has slightly higher reservoir quality than F3 (Fig. 4.4). Hence, the inference drawn was facies F6 formed after parts of F3 undergone diagenetic alteration to yield secondary porosity although not significant enough to cause higher porosity facies.

• Facies F4 is abundantly distributed in the shelf margin zone of the Wellington field part of the study area (Fig. 4.18b). Most of it coincides with the medium porosity (class 2) facies with average porosity between 8% to 12%. These facies also align with the lineament ‘N’ delineated in figure 4.18a. In addition, the facies centroid Euclidean distance matrix shows facies F4 is closest to facies F3 (6 units) and F6 (6.2 units) (Fig. 4.18c). Hence, the inference that facies F4 is a secondary petrophysical(porosity) facies generated by the reworking of facies F3 and F6 induced by the reactivation of the lineament ‘N.’

• Facies F1 and F2 (Fig. 4.18b) coincide with high porosity (class 1) facies (Fig. 4.18a). Moreover, from the distance matrix in figure 4.18c, facies F1 and F2 are closest (4.9 units); hence, the inference of a possible lower member porosity sub-class within the high porosity (Class 1) facies.

• Facies F5 is abundant in the Anson-Bates part of the shelf facies (Fig. 4.18b). It coincides with high porosity (Class 1) and low porosity facies (Class 3) in figure 4.18a. Its facies centroid distance is relatively far from the remaining facies (Fig. 4.18c). Hence, the inference of diagenetic facies with no petrophysical imprint within the reservoir.

• Facies F7 is also distinctive within the F3 facies dominant in the Wellington field part of the shelf margin facies (Fig. 4.18b). It trends roughly perpendicular (NW-SE) to the prevailing trend of facies F3 (NE-SW) in which it is embedded. In addition, its facies' centroid distances are farthest from all the facies delineated (Fig. 4.18c). Therefore, it could be an anomaly worth penetrating to uncover further details.

Notwithstanding the existence of evaporites in the reservoir, the relative proportions to that of Dolomite, Calcite, and Quartz is minimal; hence, it has no imprint on the seismic facies classes responsive to the lateral distribution of mineralogy and petrophysics (porosity) within the Mississippian reservoir.

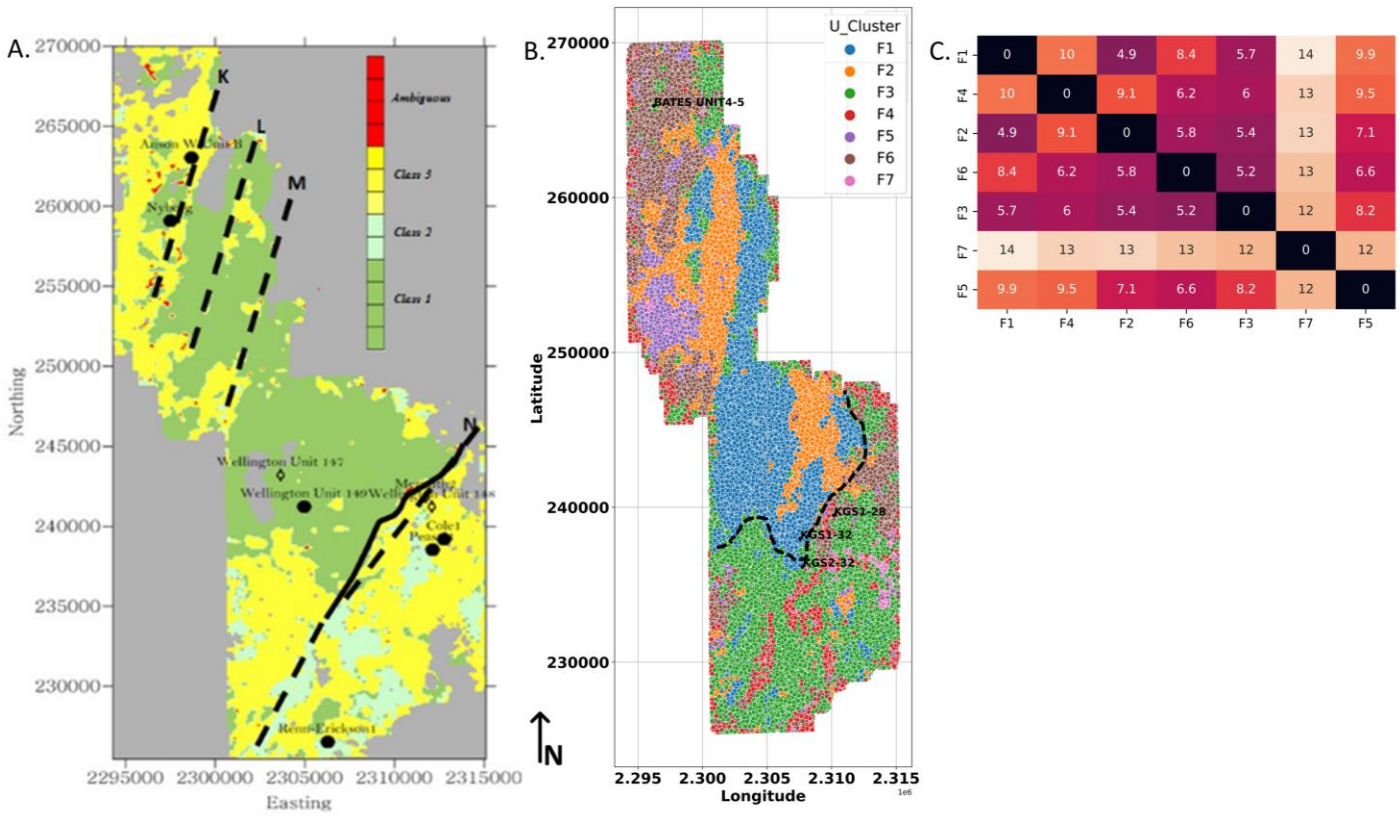

Figure 4.18 (A) Petrophysical(porosity) facies map with delineated lineaments(black dashed lines) by Ohl & Raef (2014), (B) Seismic facies map with delineated shelf edge(black dashed line) and wells containing mineral proportion and reservoir quality data, and (C) Euclidean distance matrix for the centroids of seismic facies in (B).

Chapter 5 - Conclusion and Recommendations

This study has presented delineated seismic facies and unsupervised machine learning modeling workflow that can be utilized as a baseline to monitor CO2 injected into the Mississippian reservoir at the Wellington and Anson-Bates fields through 4D seismic data surveys.

The seismic facies F1 and F2 cover highly porous zones in the study area. Judging from their relatively extensive lateral coverage with possible structural four-way closure traps existent from the time structure of the Mississippian reservoir at the coverage area, that zone is recommended as a potential zone within the Mississippian reservoir to be simulated for CO2 plume migration during EOR. The seismic facies delineated in this study are controlled by a complex blend of petrophysical (porosity), depositional and diagenetic factors. However, the limitation of insufficient well core data for the wells made it challenging to determine the dominant factor on a particular seismic facies class. Further, utilizing two different distance-based clustering algorithms provided the interpreter qualitative validation added to domain knowledge on carbonate depositional geometry to streamline multiple clusters to that representative of the underlying geological reservoir. Resolution enhancement and spectral decomposition of the data also improved the data quality, resulting in relatively finer facies boundaries and lateral distribution.

Finally, to further understand the seismic facies control to a more precise level and its effects on carbon storage, more core log data and rock thin section analyses are recommended to be integrated into the study. This will leverage the lateral resolution strength of the seismic facies with the vertical resolution strength of core data analysis to produce a higher-resolution characterization of the reservoir.

References

Arthur, D., & Vassilvitskii, S. (2006). K-means++: The advantages of careful seeding. *Stanford*.

Baines, S. J., & Worden, R. H. (2004). Geological storage of carbon dioxide. *Geological Society Special Publication*, *233*(December 2008), 1–6. https://doi.org/10.1144/GSL.SP.2004.233.01.01

Barnes, A. E. (2006). Too many seismic attributes ? *CSEG Recorder*, *31*(3), 41–46.

Barnes, A. E., & Laughlin, K. J. (2002). Investigation of methods for unsupervised classification of seismic data. *2002 SEG Annual Meeting*.

Belyadi, H., & Haghighat, A. (2021). Unsupervised machine learning: clustering algorithms. In *Machine Learning Guide for Oil and Gas Using Python* (Issue Ml). https://doi.org/10.1016/b978-0-12-821929-4.00002-0

Bickle, M. J. (2009). Geological carbon storage. *Nature Geoscience*, *2*(12), 815–818. https://doi.org/10.1038/ngeo687

Brown, A. R. (2001). Understanding seismic attributes. *Geophysics*, *66*(1), 47–48. https://doi.org/10.1190/1.1444919

Buchanan, R., & Carr, T. R. (2008). *Kansas Geological Survey*. *27*, 1–4.

Burnett, M. D., Castagna, J. P., Méndez-Hernández, E., Rodríguez, G. Z., García, L. F., Martínez Vázquez, J. T., Avilés, M. T., & Villaseñor, R. V. (2003). Application of spectral decomposition to gas basins in Mexico. *The Leading Edge*, *22*(11), 1130–1134. https://doi.org/10.1190/1.1634918

Burns, S., & Street, K. (2005). Spectral decomposition highlights faults. *Hart's E&P*, *March*.

Chen, G., Matteucci, G., Fahmy, B., & Finn, C. (2008). Spectral-decomposition response to reservoir fluids from a deepwater West Africa reservoir. *Geophysics*, *73*(6).

https://doi.org/10.1190/1.2978337

Chopra, S., Castagna, J. P., & Portniaguine, O. (2006). Seismic Resolution and Thin Bed Reflectivity Inversion. *CSEG Recorder*, 19–25.

Chopra, S., & Marfurt, K. J. (2008). Emerging and future trends in seismic attributes. *Leading Edge (Tulsa, OK)*, *27*(3), 298–318. https://doi.org/10.1190/1.2896620

Chopra, S., & Marfurt, K. J. (2020). Unsupervised Machine Learning Applications for Seismic Facies Classification. *SPE/AAPG/SEG Unconventional Resources Technology Conference 2020, URTeC 2020*, 1–8. https://doi.org/10.15530/urtec-2019-557

Chopra, S., Marfurt, K. J., & Misra, S. (2010). Seismic attributes on frequency-enhanced seismic data. *Society of Exploration Geophysicists International Exposition and 80th Annual Meeting 2010, SEG 2010*, 1462–1466. https://doi.org/10.1190/1.3513117

de Amorim, R. C. (2015). Feature Relevance in Ward's Hierarchical Clustering Using the Lp Norm. *Journal of Classification*, *32*(1), 46–62. https://doi.org/10.1007/s00357-015-9167-1

Dowdell, B. L., Kwiatkowski, J. T., & Marfurt, K. J. (2013). Seismic characterization of a Mississippi Lime resource play in Osage County, Oklahoma, USA. *Interpretation*, *1*(2), SB97–SB108. https://doi.org/10.1190/INT-2013-0026.1

El Bouchefry, K., & de Souza, R. S. (2020). Learning in Big Data: Introduction to Machine Learning. In *Knowledge Discovery in Big Data from Astronomy and Earth Observation: Astrogeoinformatics*. Elsevier Inc. https://doi.org/10.1016/B978-0-12-819154-5.00023-0

Gutschick, R. C., & Sandberg, C. A. (1983). Mississippian continental margins of the conterminous United States. *The Shelfbreak: Critical Interface on Continental Margins*, *33*, 79–96. https://doi.org/10.2110/pec.83.06.0079

Hartigan, J. A. (2015). Statistical Clustering. *International Encyclopedia of the Social &*

Behavioral Sciences: Second Edition, 392–396. https://doi.org/10.1016/B978-0-08-097086-8.42176-8

He, Y., Cao, J., Lu, Y., Gan, Y., & Lv, S. (2018). *Shale seismic facies recognition technology based on sparse autoencoder*. *April*, 1744–1748. https://doi.org/10.1190/igc2018-428

Jung Yoon, W., & Farfour, M. (2012). Spectral decomposition aids AVO analysis in reservoir characterization: A case study of Blackfoot field, Alberta, Canada. *Computers and Geosciences*, *46*, 60–65. https://doi.org/10.1016/j.cageo.2012.04.012

Karsli, H., & Dondurur, D. (2013). A procedure to reduce side lobes of reflection wavelets: A contribution to low-frequency information. *Journal of Applied Geophysics*, *96*, 107–118. https://doi.org/10.1016/j.jappgeo.2013.07.002

Lane, H. R., & De Keyser, T. L. (1980). Paleogeography of the Late Early Mississippian (Tournaisian 3) in the central and southwestern United States. *Paleozoic Paleogeography of West-Central United States: Rocky Mountain Paleogeography Symposium 1*, *6*, 149–162.

Liu, J., Yang, D., & Liu, D. (2018). Seismic amplitude attributes selection based on 3D model. *SEG Technical Program Expanded Abstracts*, 3377–3381. https://doi.org/10.1190/segam2018-2995841.1

Liu, S.-Y., Ying, M.-X., Wan-Yuan, Yue, S., Wang, R., Song*, W., & Niu, Y. (2020). *Unsupervised seismic facies analysis based on waveform Agglomerative hierarchical clustering*. *November 2019*, 22–25. https://doi.org/10.1190/iwmg2019_06.1

Maimon, O., & Rokach, L. (2010). *Data mining and knowledge discovery handbook* (L. Rokach (ed.); 2nd ed.). Springer Science+Business Media. https://doi.org/DOI 10.1007/978-0-387-09823-4_14

Manenti, R. R., Souza, W. E., & Porsani, M. J. (2018). Spectral whitening based on the singular

spectral analysis method. *Journal of Geophysics and Engineering*, *15*(4), 1460–1469. https://doi.org/10.1088/1742-2140/aab274

Masaferro, J. L., Bourne, R., & Jauffred, J.-C. (2003). 3D visualization of carbonate reservoirs. *The Leading Edge*, *22*(1), 18–25. https://doi.org/https://doi.org/10.1190/1.1542751

Mazzullo, S. J., Wilhite, B. W., Boardman, D. R., Morris, B. T., & Godwin, C. J. (2019). Lithostratigraphy, Biostratigraphy, Stratigraphic Architecture, and Depositional Systems in Lower to Middle Mississippian Strata on the Western Flank of the Ozark Dome, Midcontinent U.S.A. *Mississippian Reservoirs of the Midcontinent*, 25–57. https://doi.org/10.1306/13632141m116257

Ming, M., & Chiang, T. (2010). Intelligent Choice of the Number of Clusters in K-Means Clustering: An Experimental Study with Different Cluster Spreads. *Journal of Classification*, *190*(September), 173–190. https://doi.org/10.1007/s00357-010-

Montgomery, S. L., Mullarkey, J. C., Longman, M. W., Colleary, W. M., & Rogers, J. P. (1998). Mississippian “Chat” Reservoirs, South Kansas: Low-Resistivity Pay in a Complex Chert Reservoir. *AAPG Bulletin*, *82 (1998)*(2), 187–205. https://doi.org/10.1306/1D9BC3C7-172D-11D7-8645000102C1865D

Murtagh, F., & Legendre, P. (2014). Ward’s Hierarchical Agglomerative Clustering Method: Which Algorithms Implement Ward’s Criterion? *Journal of Classification*, *31*(3), 274–295. https://doi.org/10.1007/s00357-014-9161-z

O’Neill, S. (2020). Global CO2 Emissions Level Off in 2019, with a Drop Predicted in 2020. *Engineering*, *6*(9), 958–959. https://doi.org/10.1016/j.eng.2020.07.005

Ohl, D., & Raef, A. (2014). Rock formation characterization for carbon dioxide geosequestration: 3D seismic amplitude and coherency anomalies, and seismic

petrophysical facies classification, Wellington and Anson-Bates Fields, Kansas, USA. *Journal of Applied Geophysics*, *103*, 221–231. https://doi.org/10.1016/j.jappgeo.2014.01.017

Partyka, G., Gridley, J., & Lopez, J. (1999). Interpretational applications of spectral decomposition in reservoir characterization. *The Leading Edge*, *18*(3). https://doi.org/10.1190/1.1438295

Reilly, J. M., Aharchaou, M., & Neelamani, R. (2023). A brief overview of seismic resolution in applied geophysics. *Leading Edge*, *42*(1), 8–15. https://doi.org/10.1190/tle42010008.1

Rijfkogel, L. (2020). *Integrated analysis of seismic attributes and well-logs in reservoir characterization: seismic facies classification and reservoir facies mapping*. Kansas State University.

Sabeti, H., Birjand, I., & Tehran, I. (2011). Seismic facies classification using 2-D and 3-D multi-attribute hierarchical clustering algorithms. *Society of Exploration Geophysicists International Exposition and 81st Annual Meeting 2011, SEG 2011, Webb 2002*, 1160–1164.

Sabeti, H., & Nadjar, B. (2011). Seismic facies classification using 2-D and 3-D multi-attribute hierarchical clustering algorithms. *SEG Technical Program Expanded Abstracts 2011*, *Webb 2002*, 1160–1164. https://doi.org/10.1190/1.3627408

Shulakova, V., Sarout, J., Pimienta, L., Lebedev, M., Mayo, S., Clennell, M. B., & Pervukhina, M. (2017). Effect of supercritical CO2 on carbonates: Savonnières sample case study. *Geophysical Prospecting*, *65*(1), 251–265. https://doi.org/10.1111/1365-2478.12369

Siqueira, T. A., Iglesias, R. S., & Ketzer, J. M. (2017). Carbon dioxide injection in carbonate reservoirs – a review of CO2-water-rock interaction studies. *Greenhouse Gases: Science*

and Technology, *7*, 802–816. https://doi.org/10.1002/ghg

Song, C., Liu, Z., Wang, Y., Xu, F., Li, X., & Hu, G. (2018). Adaptive phase k-means algorithm for waveform classification. *Exploration Geophysics*, *49*(2), 213–219. https://doi.org/10.1071/EG16111

Tan, Y., Li, Q., Xu, L., Ghaffar, A., Zhou, X., & Li, P. (2022). A critical review of carbon dioxide enhanced oil recovery in carbonate reservoirs. *Fuel*, *328*(April). https://doi.org/10.1016/j.fuel.2022.125256

Theodoridis, S., & Koutroumbas, K. (2009). Clustering Algorithms II: Hierarchical Algorithms. In *Pattern Recognition* (pp. 653–700). https://doi.org/10.1016/b978-1-59749-272-0.50015-3

Wang, Y. (2012). Reservoir characterization based on seismic spectral variations. *74th European Association of Geoscientists and Engineers Conference and Exhibition 2012 Incorporating SPE EUROPEC 2012: Responsibly Securing Natural Resources*, *77*(6), 1558–1562. https://doi.org/10.3997/2214-4609.20148757

Watney, W. L., Bhattacharya, S., Gerlach, P., Rush, J., Hansen, T., Nicholson, L., Smith, A., Hedke, D., Nissen, S., Raef, A., Xia, J., Koger, D., Baker, R., & Victorine, J. (2011). Evaluation of CO 2 Sequestration Potential in Ozark Plateau Aquifer System (OPAS) in Southern Kansas - Initial Studies. *Search and Discovery*. http://www.kgs.ku.edu/PRS/Ozark/Reports/2011/ndx_watney.pdf

Watney, W. L., Guy, W. J., & Byrnes, A. P. (2001). Characterization of the Mississippian chat in South-central Kansas. *AAPG Bulletin*, *85*(1), 85–113. https://doi.org/10.1306/8626c767-173b-11d7-8645000102c1865d

Wethington, N. W., & Pranter, M. J. (2018). Stratigraphic architecture of the Mississippian limestone through integrated electrofacies classification, Hardtner field area, Kansas and

Oklahoma. *Interpretation*, *6*(4), T1095–T1115. https://doi.org/10.1190/INT-2018-0042.1

Wilson, E. N., Watney, W. L., & Grammer, G. M. (2019). An Overview of the Giant Heterogeneous Mississippian Carbonate System of the Midcontinent: Ancient Structure, Complex Stratigraphy, Conventional Traps, and Unconventional Technology in a High Fluid Volume World, in G. M. Grammer, J. M. Gregg, J. O. Pucket. *AAPG Memoir*, pp. *122*, 1–24. https://doi.org/10.1306/13632140m1163784

Wrona, T., Pan, I., Gawthorpe, R. L., & Fossen, H. (2018). Seismic facies analysis using machine learning. *Geophysics*, *83*(5), O83–O95. https://doi.org/10.1190/geo2017-0595.1

Yilmaz, O. (2001). *Seismic Data Analysis: Processing, Inversion, and Interpretation of Seismic Data (Investigations in Geophysics)*. Tulsa, OK: Society of Exploration Geophysicists. https://doi.org/https:// doi.org/10.1190/1.9781560801580

Zhao, T., Jayaram, V., Roy, A., & Marfurt, K. J. (2015). A comparison of classification techniques for seismic facies recognition. *Interpretation*, *3*(4), SAE29–SAE58. https://doi.org/10.1190/INT-2015-0044.1

Zheng, S. (2020). Whitening Processing of Seismic Signal Spectrum Based on SSGST. *International Journal of Computer Applications Technology and Research*, *9*(4), 130–132. https://doi.org/10.7753/ijcatr0904.1002

Appendix A - Cross plots of Seismic Attributes

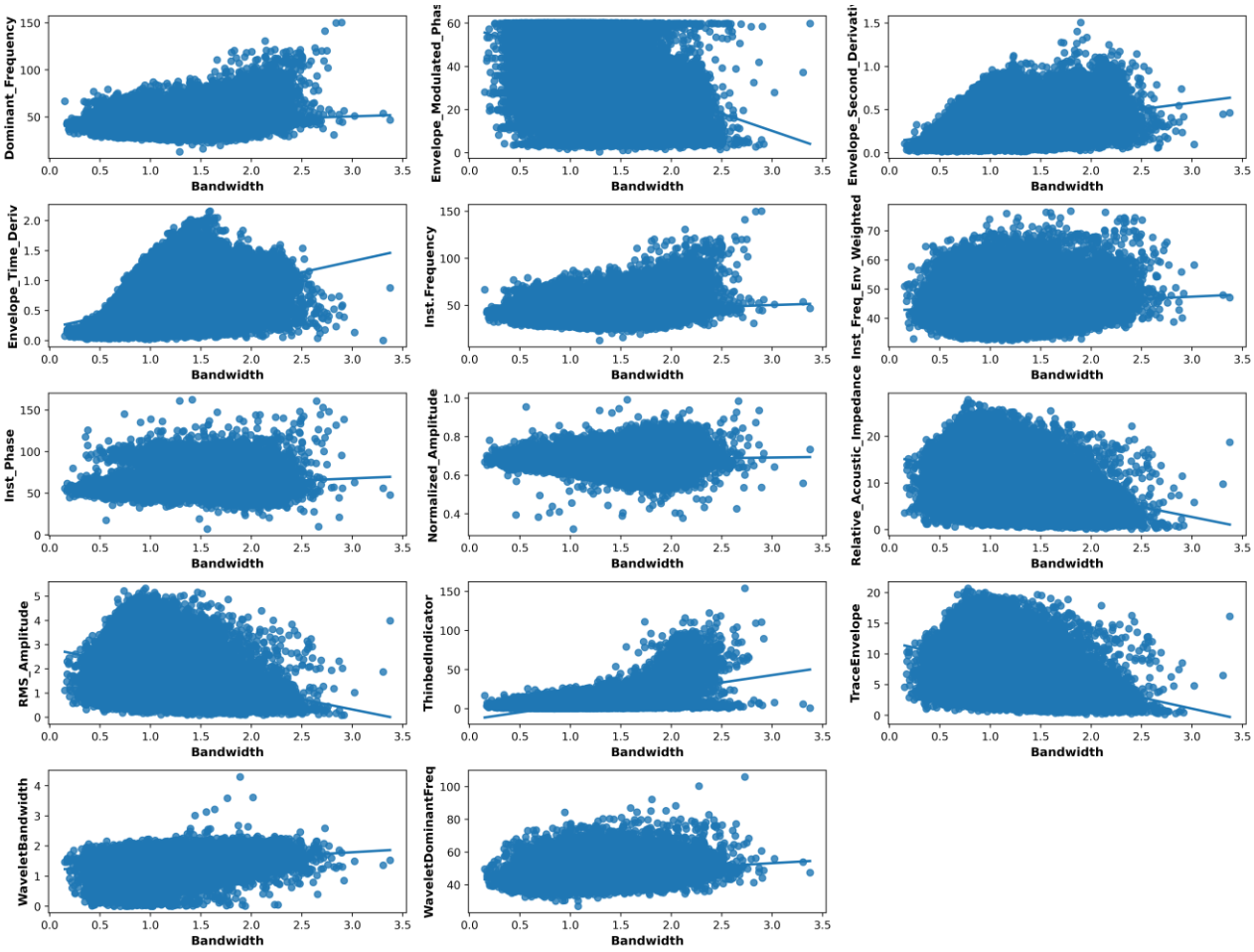

Figure A.1 Cross plot of attribute Bandwidth with the other attributes for features selection.

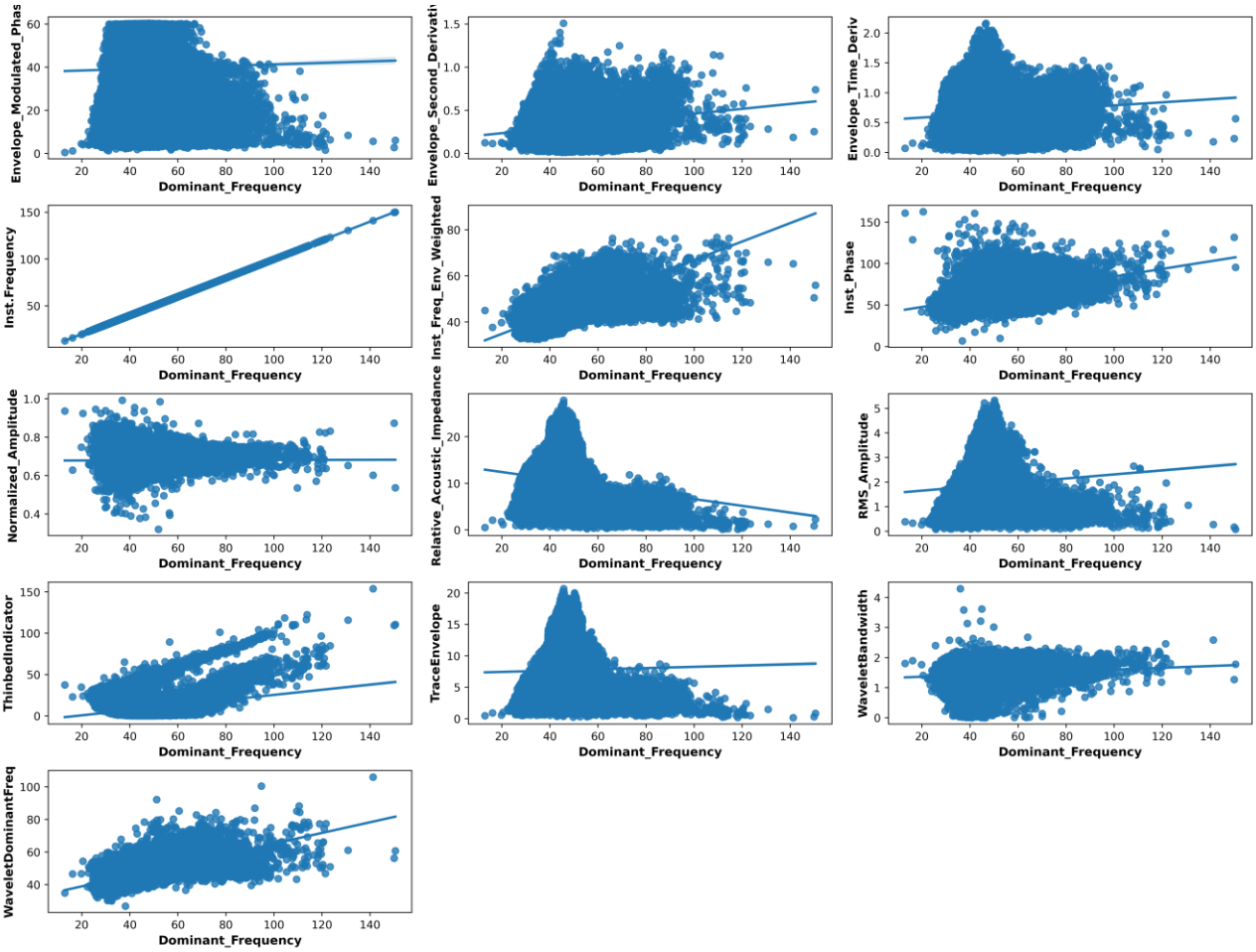

Figure A.2 Cross plot of attribute Dominant Frequency with other attributes for features selection without repetition of plots existent in preceding cross plot.

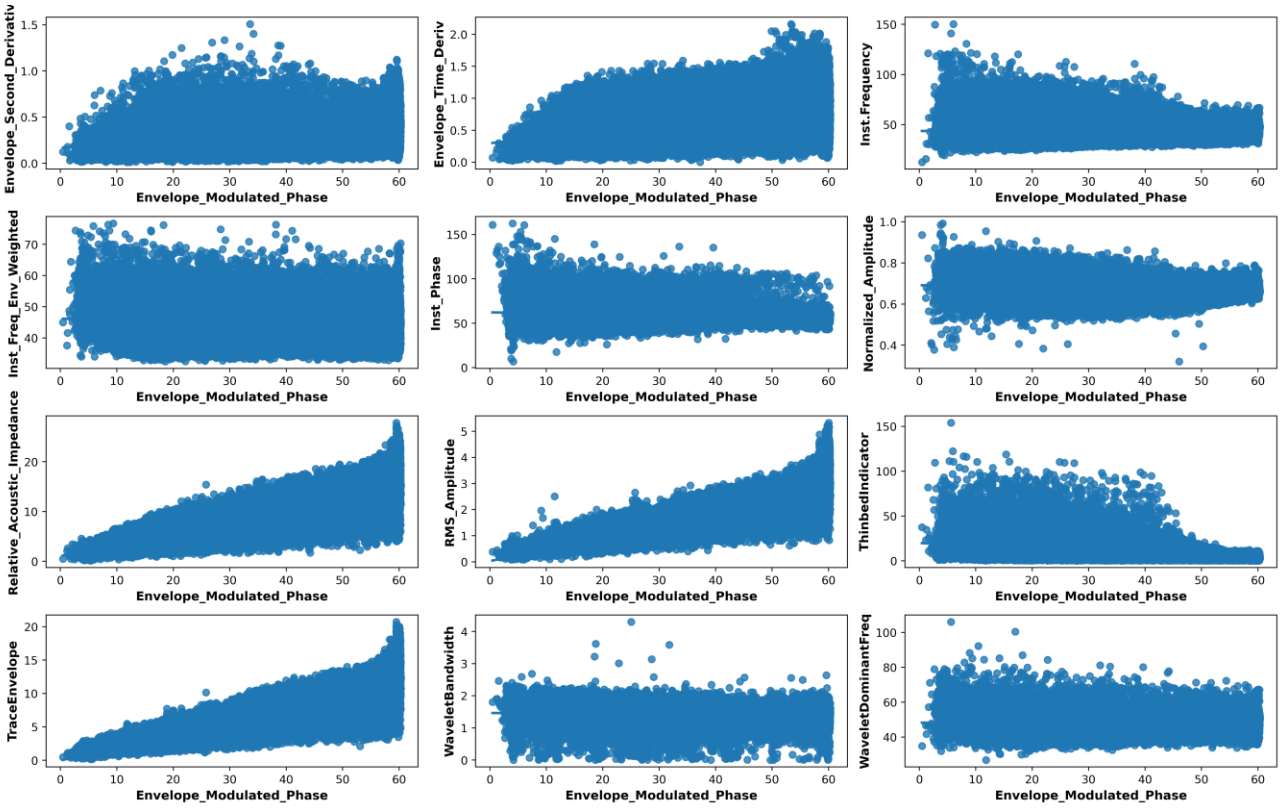

Figure A.3 Cross plot of attribute Envelope Modulated Phase with other attributes for features selection without repetition of plots existent in preceding cross plot.

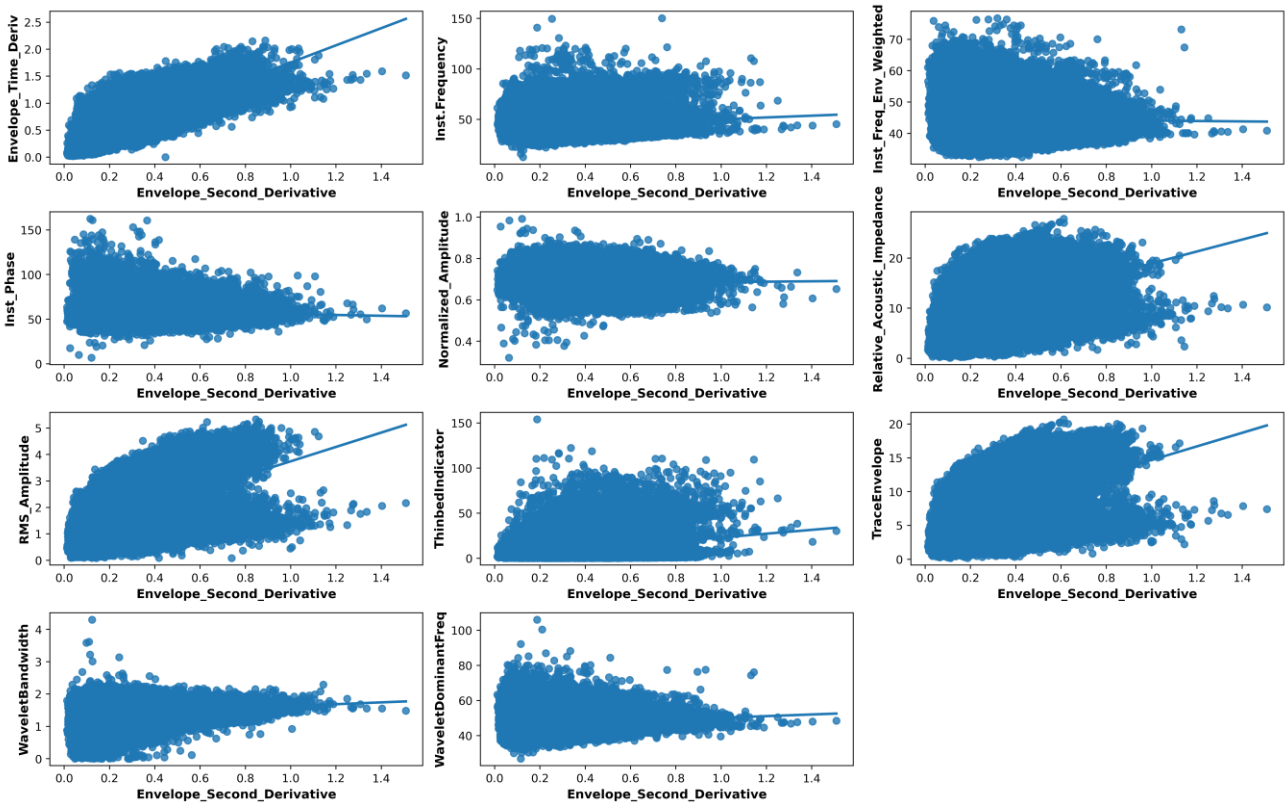

Figure A.4 Cross plot of attribute Envelope Second Derivative with other attributes for features selection without repetition of plots existent in preceding cross plot.

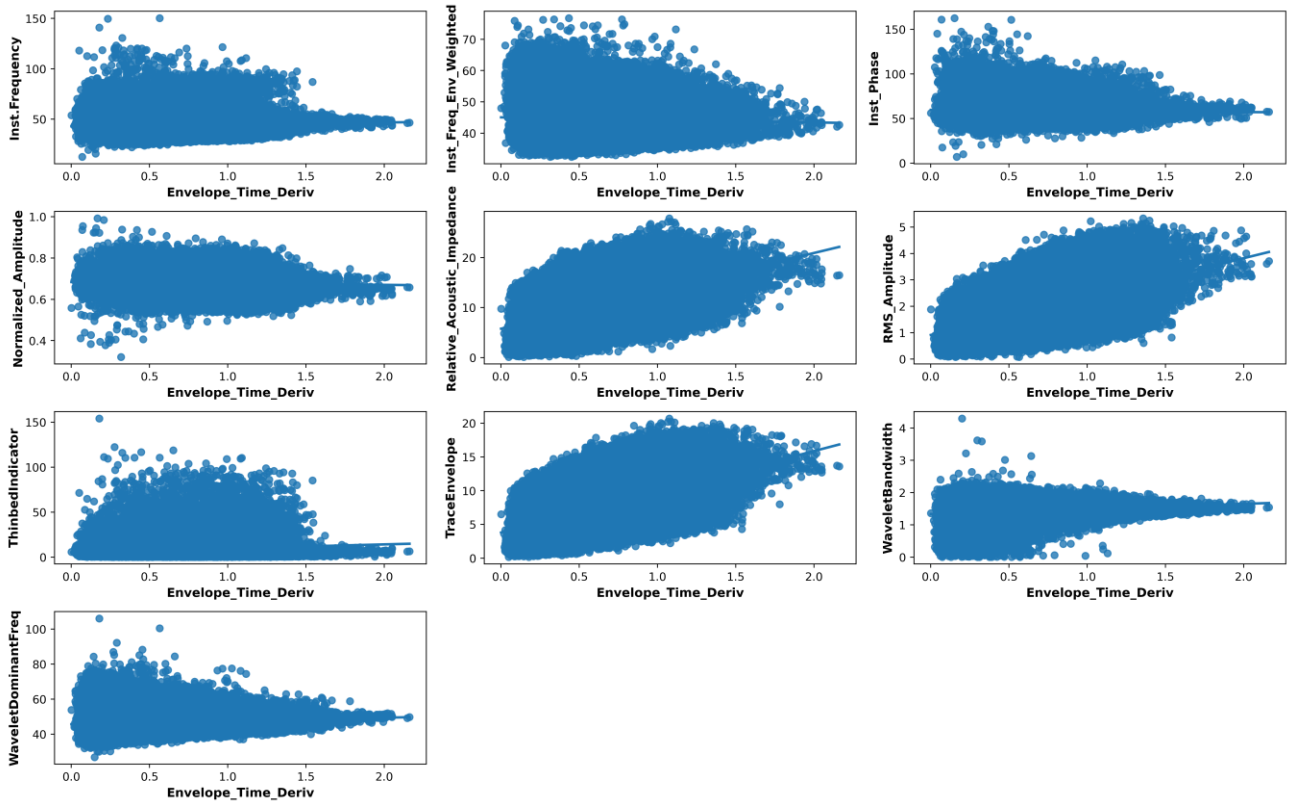

Figure A.5 Cross plot of attribute Envelope Time Derivative with other attributes for features selection without repetition of plots existent in preceding cross plot.

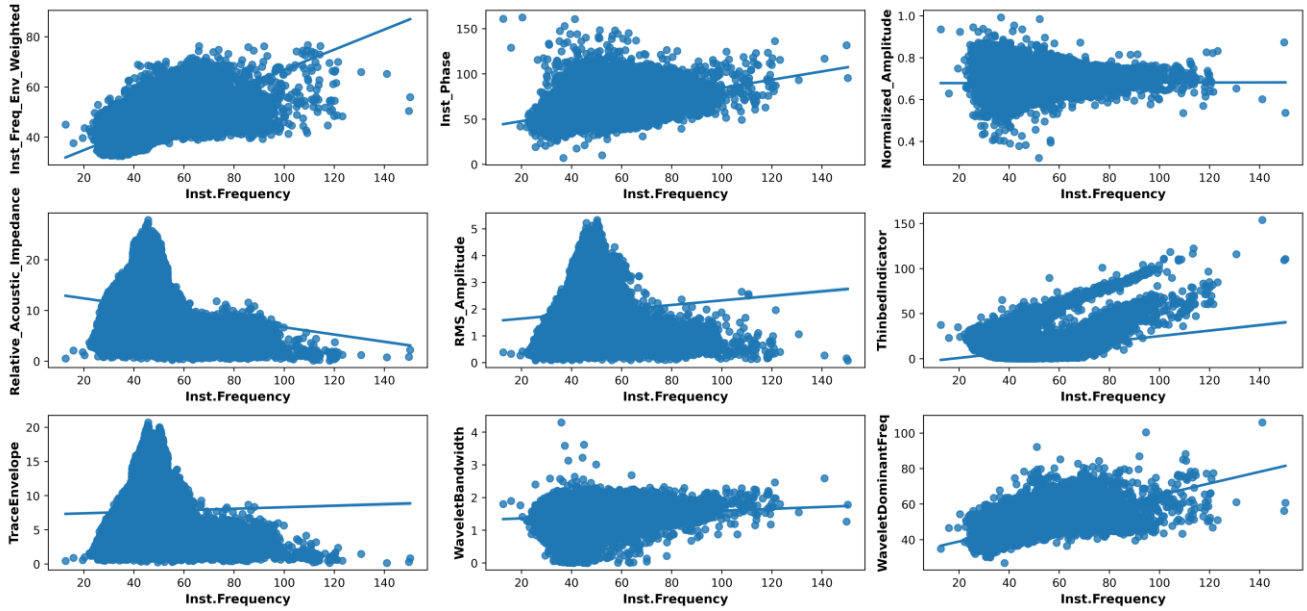

Figure A.6 Cross plot of attribute Instantaneous Frequency with other attributes for features selection without repetition of plots existent in preceding cross plot.

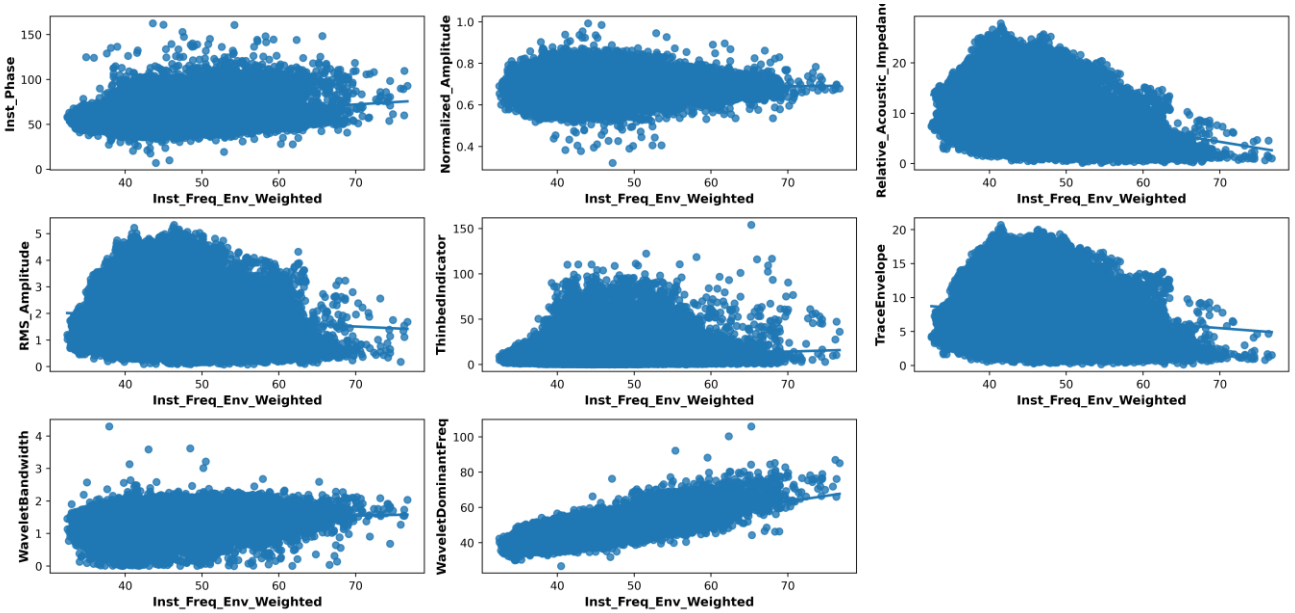

Figure A.7 Cross plot of attribute Instantaneous Frequency Envelope Weighted with other attributes for features selection without repetition of plots existent in preceding cross plot.

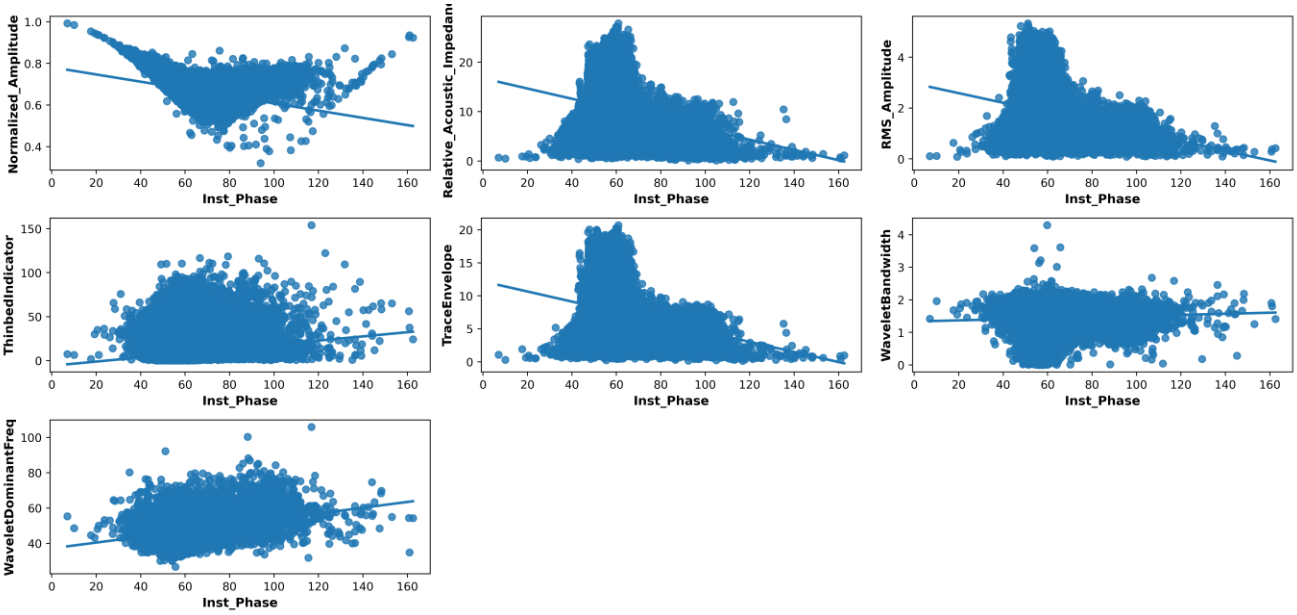

Figure A.8 Cross plot of attribute Instantaneous Phase with other attributes for features selection without repetition of plots existent in preceding cross plot.

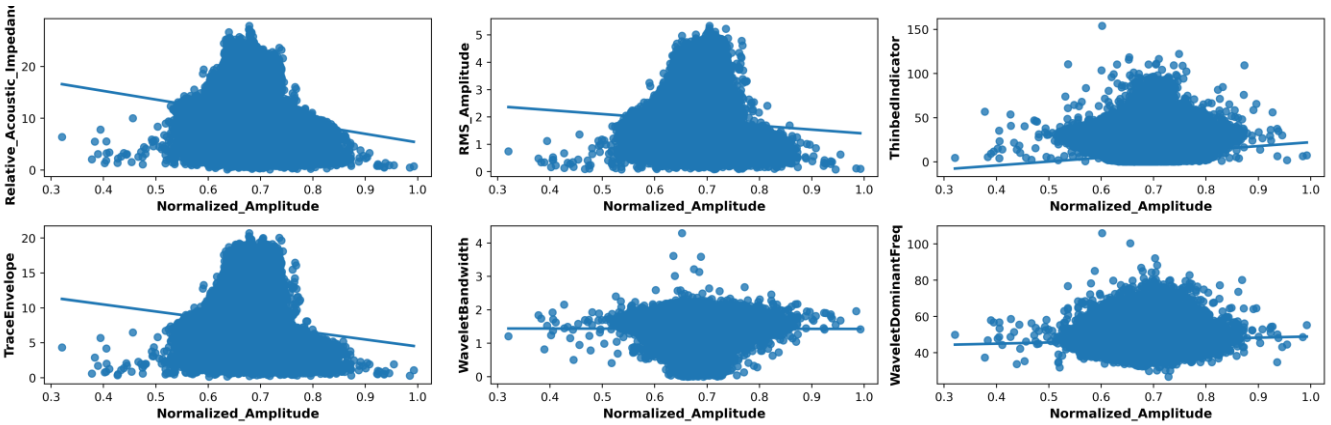

Figure A.9 Cross plot of attribute Normalized Amplitude with other attributes for features selection without repetition of plots existent in preceding cross plot.

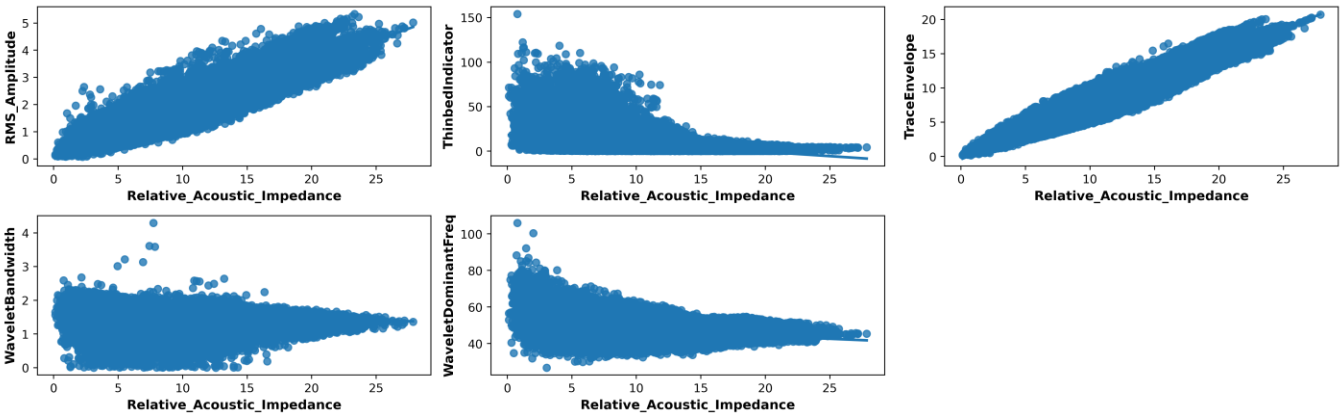

Figure A.10 Cross plot of attribute Relative Acoustic Impedance with other attributes for features selection without repetition of plots existent in preceding cross plot.

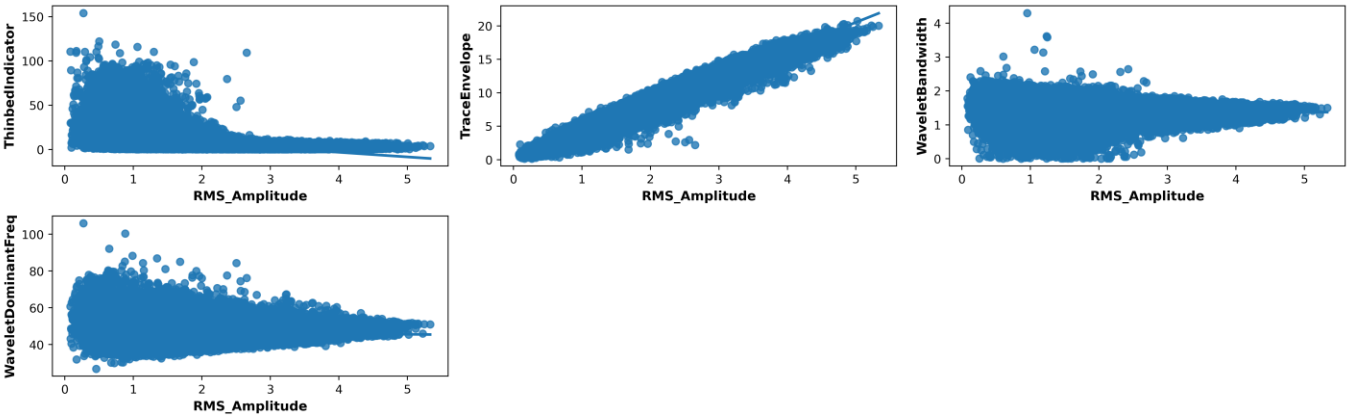

Figure A.11 Cross plot of attribute RMS Amplitude with other attributes for features selection without repetition of plots existent in preceding cross plot.

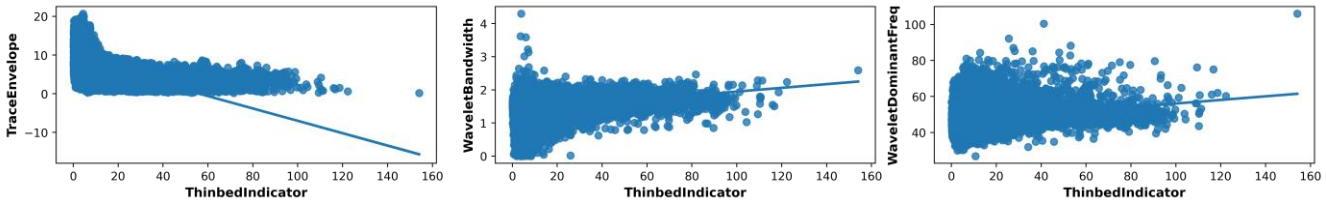

Figure A.12 Cross plot of attribute Thin Bed Indicator with other attributes for features selection without repetition of plots existent in preceding cross plot.